

1 Late Cretaceous Channel Flow In Western
2 Arizona: Implications For The Ancestral
3 Evolution of Metamorphic Core Complexes

4 Thomas N Lamont^{1*}, Shane Scoggin², Johannes Haemmerli²,
5 Gabe Epstein³, Alex Scandore¹, Meaghan Boyle¹, Michael Wells¹

6 ^{1*}Department of Geoscience, University of Nevada Las Vegas, 4505 S.
7 Maryland Parkway, Las Vegas, 89154, NV, USA.

8 ²Department of Geology, Washington State University, Pullman, 99163,
9 WA, USA.

10 ³School of Earth and Sustainability, Northern Arizona University,
11 Flagstaff, 86001, AZ, USA.

12 *Corresponding author(s). E-mail(s): thomas.lamont@unlv.edu;

13 **Abstract**

14 The origin of ancestral 'extensional' shear fabrics in metamorphic core complexes
15 (MCCs) in the Colorado River Extensional Corridor remains a tectonic mystery.
16 Here we show that Late-Cretaceous metamorphic rocks and migmatites in the
17 Harcuvar-Harquahala and Granite Wash Mountains MCCs reached peak meta-
18 morphic conditions of ca. 0.75 GPa and 780°C and were extruded towards the
19 SW onto lower grade metamorphic rocks via 'channel flow' between ca. 76–70
20 Ma, ~40 Myrs before regional extension. The channel is bounded by a top-NE
21 'extensional' roof shear zone and a top-SW thrust-sense base, associated with
22 an inverted metamorphic gradient. U-(Th)-Pb and Rb-Sr geochronology con-
23 firms that shearing at the roof and base occurred concurrently. To explain these
24 features, we propose that low-angle subduction of the Farallon plate released
25 volatiles directly into the base of the North American crust, which induced water-
26 fluxed crustal melting and rheological weakening, facilitating flow of deep crustal
27 rock to shallower depths. Consequently, ancestral 'extensional' fabrics in MCCs
28 may represent the roof of an extruding channel formed in an overall contractional
29 setting.

30 **Keywords:** Metamorphic Core Complex, Channel Flow, Low-Angle Subduction,
31 Water-Fluxed Crustal Melting, Laramide Orogeny

32 INTRODUCTION

33 Metamorphic core complexes (MCCs) are characteristic features of extensional con-
34 tinental tectonics and are defined as having a high-grade metamorphic footwall that
35 is separated from an unmetamorphosed hanging wall by a low angle normal fault or
36 ductile shear zone (Figure 1; Teyssier and Whitney, 2002; Whitney et al. 2013; Platt
37 et al. 2014). However, within the footwall of many MCCs across the North American
38 Cordillera and Alpine-Himalayan belt, the timing of peak metamorphism and ductile
39 shearing significantly pre-dates the onset of regional crustal extension and sedimen-
40 tary basin formation in the hanging wall of the detachment (Figure 2). Kyanite and
41 sillimanite grade gneisses, migmatites and sometimes granulite facies rocks exposed
42 at the deepest structural levels of many MCC footwalls often demonstrate clockwise
43 pressure temperature time (P-T-t) paths associated with burial and heating of rock in
44 contractional settings, which is followed by periods of decompression and exhumation,
45 prior to regional extension (Searle and Lamont, 2019; Lamont et al. 2020; Hallet and
46 Spear, 2014; Wells et al., 2020). Shear fabrics associated with this ancestral phase of
47 exhumation are preserved within many MCCs, and are cut or captured by a younger
48 normal fault responsible for final MCC exhumation to the Earth’s surface (Hodges
49 and Walker, 1992; Wells and Hoisch, 2008; Searle and Lamont, 2019; Lamont et al.
50 2020a; Zuza et al. 2022). This capture of older, higher temperature fabrics is especially
51 prevalent in the MCCs of the Colorado River Extensional Corridor (CREC; Davis and
52 Lister, 1988; Spencer and Reynolds, 1990; Singleton and Mosher, 2012). This ancestral
53 phase of exhumation requires advection of deep crustal material before the main phase
54 of extension. However, the origin of ancestral shear fabrics preserved within the foot-
55 walls of many MCCs remains poorly understood. Because these fabrics predate strain
56 indicators associated with final exhumation, they may provide important insights into
57 the dynamic strain and stress regimes that operated within the continental lithosphere
58 during orogenesis.

59 One possibility is that the ancestral shear fabrics represent normal faulting and
60 crustal extension either during orogenic collapse (Dewey, 1988) or in a locally exten-
61 sional setting within a zone of overall convergence (Dalmayrac and Molnar, 1981;
62 Figure 3A). Evidence in support of these extensional hypotheses would be preserva-
63 tion of only normal-sense shear indicators coeval with decompression. In other words,
64 as the rocks moved upward towards the earth’s surface from higher pressure to lower
65 pressure, their older high-pressure minerals should have been overprinted or replaced
66 by lower-pressure mineral assemblages that are associated with only normal sense
67 shear indicators. Pure shear, uniform (with depth) lithospheric extension increases
68 the crustal geotherm at a rate proportional to conductive heat-loss due to exhuma-
69 tion of rock at all crustal levels (e.g., Ruppel et al., 1988). This does not cause any
70 net-heating of rock, but rather cooling of rock or delayed cooling during exhumation,
71 depending on the magnitudes and rates of extension. Depth dependent extension, with
72 smaller magnitudes of extension in the crust (β) and larger magnitudes of extension in
73 the mantle (γ), results in deep crustal heating (e.g. Royden and Keen, 1980; Royden,
74 1996; Lamont et al. 2023). Compared to uniform extension, increasing magnitudes of
75 extension with depth would produce: A) a higher metamorphic field gradient increas-
76 ing with structural depth beneath the detachment, and B) alkalic volcanism due to

Key Features of Metamorphic Core Complexes (MCCs)

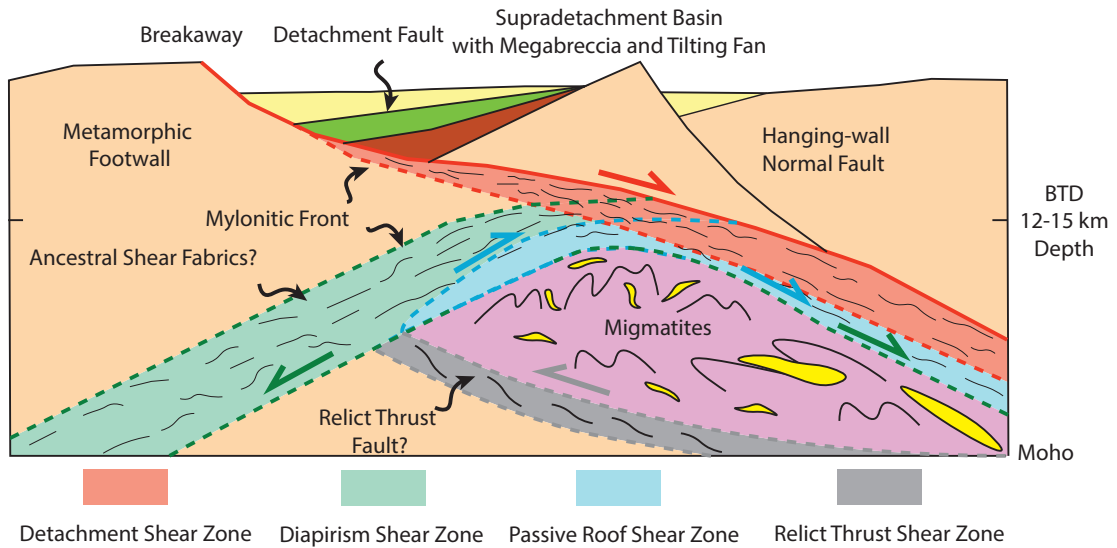


Fig. 1: Cartoon sketch showing the key features of metamorphic core complexes (MCCs) after Zuza et al. (2022). Note the ancestral shear fabrics and shear zones within the metamorphic footwall which are discordant to the detachment fault.

77 melting the lithospheric mantle from increased asthenospheric heat flow. Both exten-
 78 sional cases would also lead to development of a sedimentary basin in the the hanging
 79 wall of the detachment fault. Perplexingly, in most MCCs, such upper crustal exten-
 80 sional features and volcanism are not preserved at the time of peak metamorphism and
 81 ductile shearing (Hodges and Walker, 1992). A possible explanation is a blind exten-
 82 sional allochthon model, whereby the mid-crust flows laterally bound by shear zones
 83 with opposing shear senses, leaving thinner-crust in its wake (Hodges and Walker,
 84 1992). However, the absence of these features and structural relationships cast doubt
 85 on an overall extensional origin for the ancestral shear fabrics and may challenge the
 86 interpretation that they formed in an overall extensional tectonic setting.

87 Another possibility is that these shear fabrics result from diapirism (Zuza and
 88 Cao, 2022; Figure 3B). In this model, vertical flow of low viscosity and lower density
 89 partially molten lower crust occurs due to the development of a Rayleigh-Taylor insta-
 90 bility. According to this model, one would expect to see chaotically deformed rocks
 91 within a gneiss or migmatite dome that is bound by radially divergent shear senses and
 92 lineations and steep fabrics along its margins due to upward flow of deep crustal mate-
 93 rial towards the Earth's surface. Diapirism could also occur in a tectonically quiescent
 94 setting after crustal thickening and before regional extension, as deformation is driven

95 by buoyancy contrasts likely due to partial melting of the mid to lower crust. How-
96 ever, many MCCs show uni-directional shear indicators and shallow-sub horizontal
97 plunging lineations (Lamont et al. 2020a), inconsistent with this model.

98 Alternatively, ductile extrusion of high-grade metamorphic rocks or ‘channel flow’
99 can explain the exhumation of rocks and the development of ‘extensional’ shear fabrics
100 in a wholly contractional setting (Burchfield and Royden, 1985; Beaumont et al. 2001;
101 Searle et al. 2004; Godin et al. 2006; Searle and Lamont, 2019; Figure 3C). This model
102 is defined as flow of a weak, ductile layer between relatively rigid, yet deformable,
103 material above and below. The channel’s lower boundary is defined by a thrust fault or
104 ductile shear zone, while its upper boundary consists of a normal fault or extensional
105 shear zone with a fixed hanging wall (Means, 1989), that operated simultaneously.
106 Because weak ductile material flows between relatively fixed lithologies above and
107 below, the upper and lower channel boundaries develop opposite shear senses that
108 operated simultaneously. This flow also moves hot, deep crustal rocks relative to cooler
109 rocks, which results in an inverted metamorphic gradient near the base of the channel
110 and a right-way up metamorphic gradient in the upper part of the channel. Two end-
111 member models can describe the relative motion of ductile rocks within the channel.
112 The Poiseuille flow (pipe flow) model, suggests the highest flow velocities occur in the
113 middle of the channel, while the Couette flow model suggests the highest velocities
114 occur either along the top or the base of the channel (Law et al. 2004, 2011; Grujic et
115 al. 1996, Klempere 2006).

116 Channel flow or ductile extrusion has been well documented in subduction com-
117 plexes that expose high-pressure metamorphic rocks juxtaposed against rocks that
118 obtained much lower metamorphic grades as thrust bound nappes or blocks within
119 a mélangé (England and Holland, 1979; Geyra et al. 2002; Agard et al. 2009; Searle
120 and Lamont, 2019; Lamont et al. 2020b). In these settings, return flow is driven by
121 the positive buoyancy contrast between subducted crustal material that is detached
122 from the down-going plate and the surrounding mantle (e.g., England and Holland,
123 1979). However, our understanding of how such a mechanism operates in continental
124 crustal settings associated with regional metamorphism remains limited, particularly
125 where buoyancy contrasts are less pronounced (e.g., Grujic et al. 1996; Beaumont et
126 al. 2001; Searle et al. 2003; Law et al. 2004, 2011; Godin et al. 2006).

127 The Greater Himalayan Series (GHS) in the high Himalaya is the best represen-
128 tation of where the channel flow model may account for the opposite shear senses
129 and metamorphic field gradients of once mid crustal metamorphic rocks. The GHS
130 is bounded along the base by the Main Central Thrust (MCT) ductile shear zone, a
131 south-verging thrust that was concomitant with an inverted metamorphic field gradi-
132 ent (Hubbard 1989; Searle et al. 2006, 2018; Jessup et al. 2008a, b). In contrast, the
133 north-dipping South Tibetan Detachment (STD) low-angle normal faults were con-
134 comitant with right-way up metamorphic isograds along the top (Caby, 1983; Burchfiel
135 et al. 1992; Searle et al. 2003; Law et al. 2004, 2011; Cottle et al. 2007, 2015; Searle
136 2010; Waters et al. 2019). Both the MCT and STD ductile shear zones were active
137 simultaneously (Godin et al. 2006) as supported by high-temperature ductile fabrics
138 and ages of metamorphism throughout the GHS above the MCT zone and beneath
139 the STD zone. The migmatite–leucogranite zone along the upper part of the GHS

140 records melting and deformation associated with southward-verging transport (Cottle
141 et al. 2009; Searle et al. 2010). It is proposed that southward directed flow was driven
142 by horizontal pressure gradients from gravitational potential energy gradients, as well
143 as a denudation front (Beaumont et al. 2001) due to rheological weakening associ-
144 ated with in-situ crustal melting as documented by GHS migmatites and leucogranites
145 (Yang et al. 2019).

146 The retro-wedge within the East Greenland Caledonides is another, albeit lesser
147 studied, example of channel flow or ductile extrusion (e.g. Hodges, 2016). Here, mid-
148 crustal upper amphibolite facies metamorphic rocks and migmatites (Gilotti et al.
149 2008; Johnston & Kylander-Clark, 2013) (referred to as the 'infrastructure') is sepa-
150 rated from low-grade metamorphic rocks in the foreland by westward verging thrust
151 faults (Leslie and Higns, 2008), which in some places have been reactivated as exten-
152 sional detachments (e.g., Andresen et al. 2007, White & Hodges 2002). In contrast,
153 the roof shear zone, that separates the upper amphibolite facies 'infrastructure' in the
154 footwall from low grade metamorphic and sedimentary rocks (referred to as the 'supra-
155 structure') in the hanging wall is an eastward dipping shallowly dipping normal fault -
156 The Fjord Region Detachment (FRD) (Andresen et al. 1998; Hartz & Andresen 1995;
157 Hartz et al. 2000, 2001; Strachan 1994; Strachan & Martin 2001; Hodges et al. 2016).

158 Here, we synthesize the field relationships and present new structural interpretation
159 and geochronology data to better understand the geodynamic processes that operated
160 within the metamorphic footwall of Harcuvar-Harquahala-Granite Wash Mountains
161 MCCs within the North American Cordillera at a latitude near $\sim 34^\circ\text{N}$. We propose
162 that the Hercules, Centennial and Harquahala Thrusts in the Harcuvar, Harquahala,
163 and Granite Wash Mountains of western Arizona represent the lower boundary of a
164 ductile channel. High-grade metamorphic rocks, migmatites, and leucogranites struc-
165 turally above these faults were transported southwestward by Late Cretaceous channel
166 flow during the onset of low-angle subduction of the Farallon Plate. These new data
167 challenge existing interpretations and provide critical new constraints on the origin
168 of ancestral subhorizontal 'extensional' shear fabrics preserved in metamorphic core
169 complexes globally.

170 **Geology of the Harcuvar Harquahala and Granite** 171 **Wash Mountains**

172 The Harcuvar, Harquahala and Granite Wash Mountains are a series of MCCs located
173 within the Colorado River extensional corridor of western Arizona in the hinterland
174 of the Sevier-Laramide Orogen. These ranges are elongate domes with NE-SW trend-
175 ing long axes and are bound by NE plunging Miocene extensional detachment faults
176 including the Bullard and Eagle Eye Detachment faults (Reynolds and Spencer, 1989;
177 Reynolds et al. 1993). The Bullard and Eagle Eye detachment faults separate the
178 unmetamorphosed Miocene volcanic rocks in the hanging walls from their metamor-
179 phic footwalls. (U-Th)/He zircon, Ar-Ar and Rb-Sr thermochronology has shown the
180 extensional detachment faults were active from ca. 22 Ma to ca. 16 Ma (Richard et
181 al., 1990; Singleton et al. 2014; Wong et al. 2023) and were responsible for the final
182 exhumation of the MCCs to the Earth's surface. However, beneath the extensional

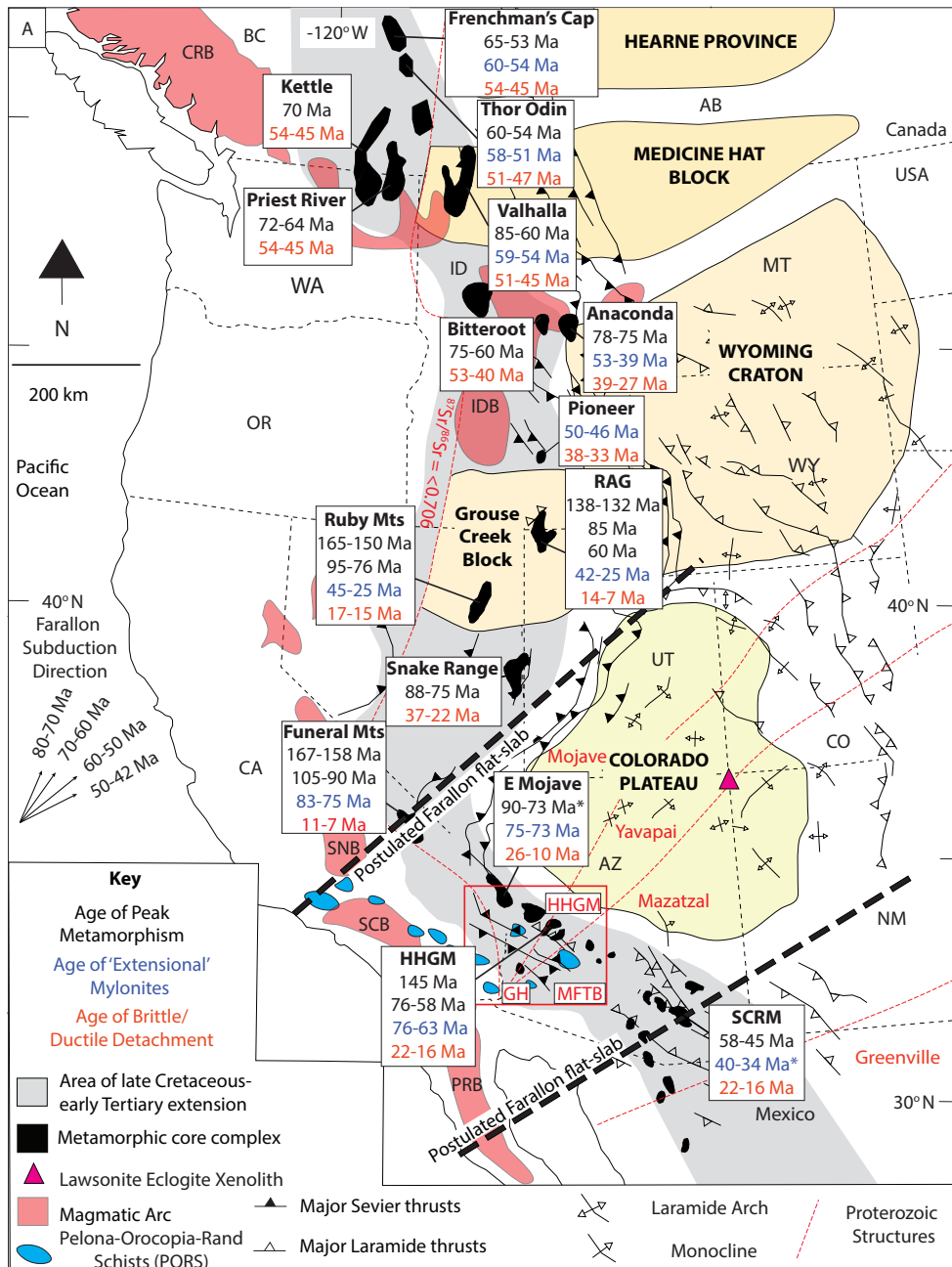


Fig. 2: Summary map of the SW USA showing ages of peak metamorphism and timing of ductile extensional shear fabrics and low temperature thermochronology related to timing of brittle extension. Location of Maria Fold Thrust Belt (MFTB), Harquahala-Harcuvar-Granite Wash Mountains (HHGM), Gavilan Hills (GH), Raft-River Albion, Grouse Creeke Mountains (RAG), SCRMs (Santa Catalina-Rincon Mountains). See supplementary material for a complete compilation and list of references.

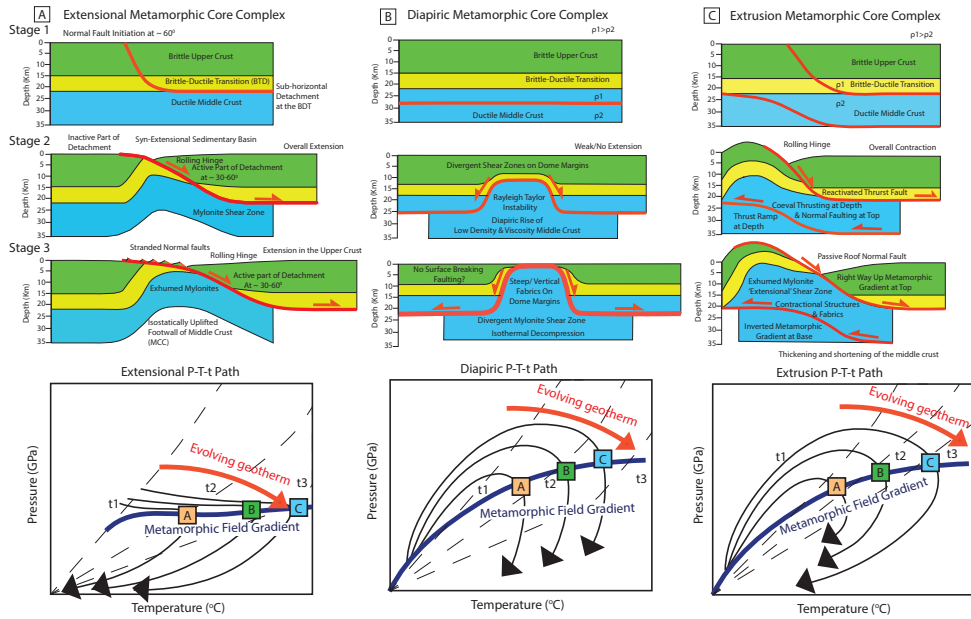


Fig. 3: Models for ancestral shear fabrics within the footwall of MCCs. A) Ductile shearing associated with a crustal scale detachment fault during regional extension, expected P-T path involving isobaric heating followed by exhumation or delayed cooling during exhumation. B) Ductile shearing on margins of a crustal scale diapir, that formed as a result of a Rayleigh Taylor instability, and expected P-T path involving isothermal decompression, C) Ductile shearing associated with a syn-convergent extrusion with a thrust fault at the base and an extensional detachment at the top of the extruding channel or wedge, and expected P-T-t path involving burial and heating from contraction followed by decompression and cooling due to extrusion related exhumation placing deeper and hotter rocks to top of shallower cooler rocks.

183 detachments, within the metamorphic footwall, a section of mid to lower crust of ~60
 184 km structural thickness is exposed.

185 This crustal section comprises high-grade metamorphic rocks including kyanite and
 186 sillimanite bearing migmatites, Proterozoic gneisses and Late Cretaceous-Paleocene
 187 peraluminous and metaluminous granites. These high grade metamorphic and Protero-
 188 zoic basement rocks belong to the overthrust crystalline southwest verging thrust
 189 sheets that define the Maria Fold-Thrust Belt (MFTB), a characteristic Laramide con-
 190 tractional feature in western Arizona and south east California (Reynolds et al. 1987;
 191 Spencer & Reynolds, 1990; Richard et al. 1994). The MFTB is an east-west trend-
 192 ing belt of greenschist-amphibolite facies metamorphic rocks characterized by largely
 193 south-vergent folds and ductile shear zones that place Jurassic and Proterozoic crys-
 194 talline rocks over Paleozoic and Mesozoic sedimentary and volcanic rocks correlative
 195 to strata observed on the Colorado Plateau and in southeastern Arizona (Spencer
 196 and Reynolds, 1990). $^{40}\text{Ar}/^{39}\text{Ar}$ step-heating analyses show the MFTB underwent
 197 regional metamorphism between ca. 90-80 Ma, likely due to overthrusting of basement

198 nappes (Knapp & Heizler, 1987). A deformed diorite, dated at ca. 86 Ma by U-Pb zir-
199 con geochronology (Saleem, 2009) and a granodiorite in the Coxcomb Mountains that
200 cuts the McCoy Mountains Formation at ca. 73.5 Ma (Barth et al. 2004), indicate
201 that thrusting occurred during the Late Cretaceous. Despite these dates, many ques-
202 tions remain, such as the precise timing and style of deformation and metamorphism
203 within the MFTB and whether this influenced subsequent MCC development. Below
204 we summarize the key geological features along a SW-NE transect through the Gran-
205 ite Wash, Harquahala and Harcuvar Mountains and integrate new thermobarometry
206 and geochronology of deformation and metamorphism with previous literature data
207 to provide new insights into the MFTB and the formation of these MCCs.

208 RESULTS

209 Field Relationships, Thermobarometry and Geochronology

210 In the Granite Wash Mountains to the far SW of the study area, the McCoy Mountains
211 Formation was deposited between ca. 129 Ma and ca. 73 Ma (Caylor et al. 2024)
212 and overlies Jurassic volcanics and Mesozoic sediments. These rocks only show low
213 grade metamorphic assemblages (muscovite-chlorite; Fig. 5J,K) and are folded into a
214 SW verging syncline, suggesting a phase of Late Cretaceous contraction shortly after
215 final sediment deposition. These rocks are overlain by a major SW verging thrust
216 fault – The Hercules Thrust – that places Proterozoic basement granites, gneisses and
217 migmatites on top of the lower grade Mesozoic greenschist facies rocks.

218 A sample of a McCoy Mountains metasediment in the immediate footwall of
219 the Hercules Thrust is characterized by the greenschist facies assemblage comprising
220 muscovite-chlorite-epidote-titanite-albite-quartz (Fig. 6G), which equilibrated at 0.36
221 ± 0.13 GPa and 503 ± 36 °C (Lamont et al. 2024; Fig. 8). In-situ Rb-Sr geochronol-
222 ogy on syn-kinematic white mica from the same sample yielded a date of 71.7 ± 12.9
223 Ma (Lamont et al. 2024), suggesting upper greenschist facies metamorphic conditions
224 occurred during SW directed thrusting.

225 In the immediate hanging wall of the Hercules Thrust, leucosomes (former melt)
226 occur within the Proterozoic basement and show top-SW asymmetry (Fig. 5H). How-
227 ever, the Granite Wash Granodiorite (ca. 72.7 Ma; U-Pb zircon age; Chapman et al.
228 2018) and the Tank Pass Ms+Grt+Bt granite (ca. 74-64 Ma; U-Pb zircon; Bryant &
229 Wooden, 2008; Wong et al. 2023) cross cut the Hercules Thrust zone, suggesting that
230 SW directed movement on the Hercules Thrust ceased by ca. 72-70 Ma.

231 Along strike to the south in the Little Harquahala Mountains, a complete section of
232 the Hercules Thrust zone is exposed. Here, the Hercules Thrust also places mylonitized
233 Proterozoic Basement gneisses on top of Jurassic volcanics and McCoy metasediments
234 (Spencer et al. 2024). Structurally above the Hercules Thrust sheet, the Centennial
235 Thrust places a sheet of Proterozoic basement and Paleozoic and Mesozoic metasedi-
236 ments over Proterozoic basement. The local presence of garnet in some metasediments,
237 suggests an increase in metamorphic grade up structural section. Continuing up section
238 in the Harquahala Mountains, the Harquahala Thrust, places an additional thrust
239 sheet of crystalline basement on top of Mesozoic metasediments and Proterozoic Har-
240 quahala Granite. Along the Harquahala Thrust, the Proterozoic basement assemblages

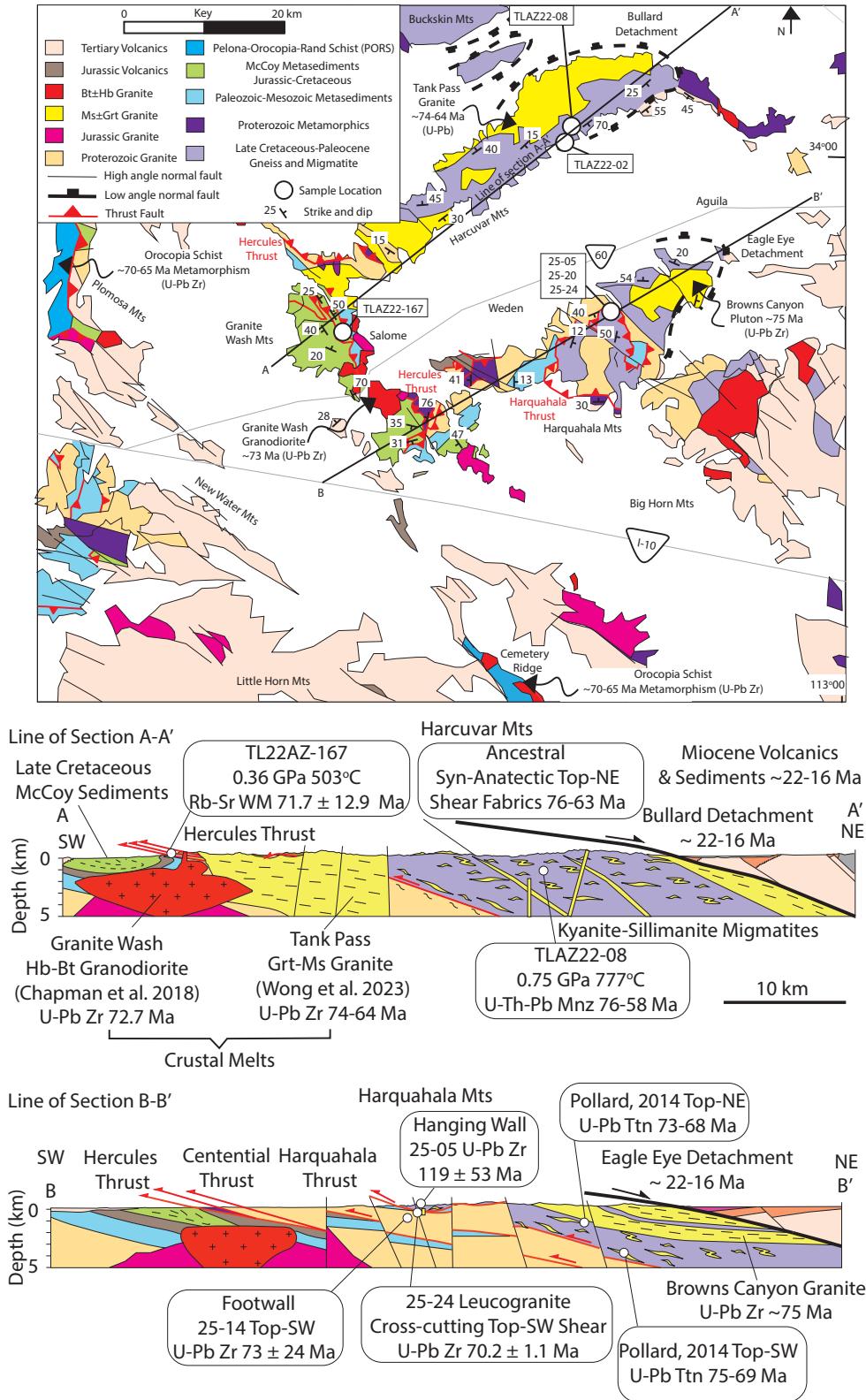


Fig. 4: Map and cross section of the Granite Wash, Harcuvar and Harquahala Mts showing sample locations, and the overall structure with inverted metamorphic field gradient at the base and top-SW shear fabrics and right-way up metamorphic field gradient and opposite top-NE shear fabrics at the top.

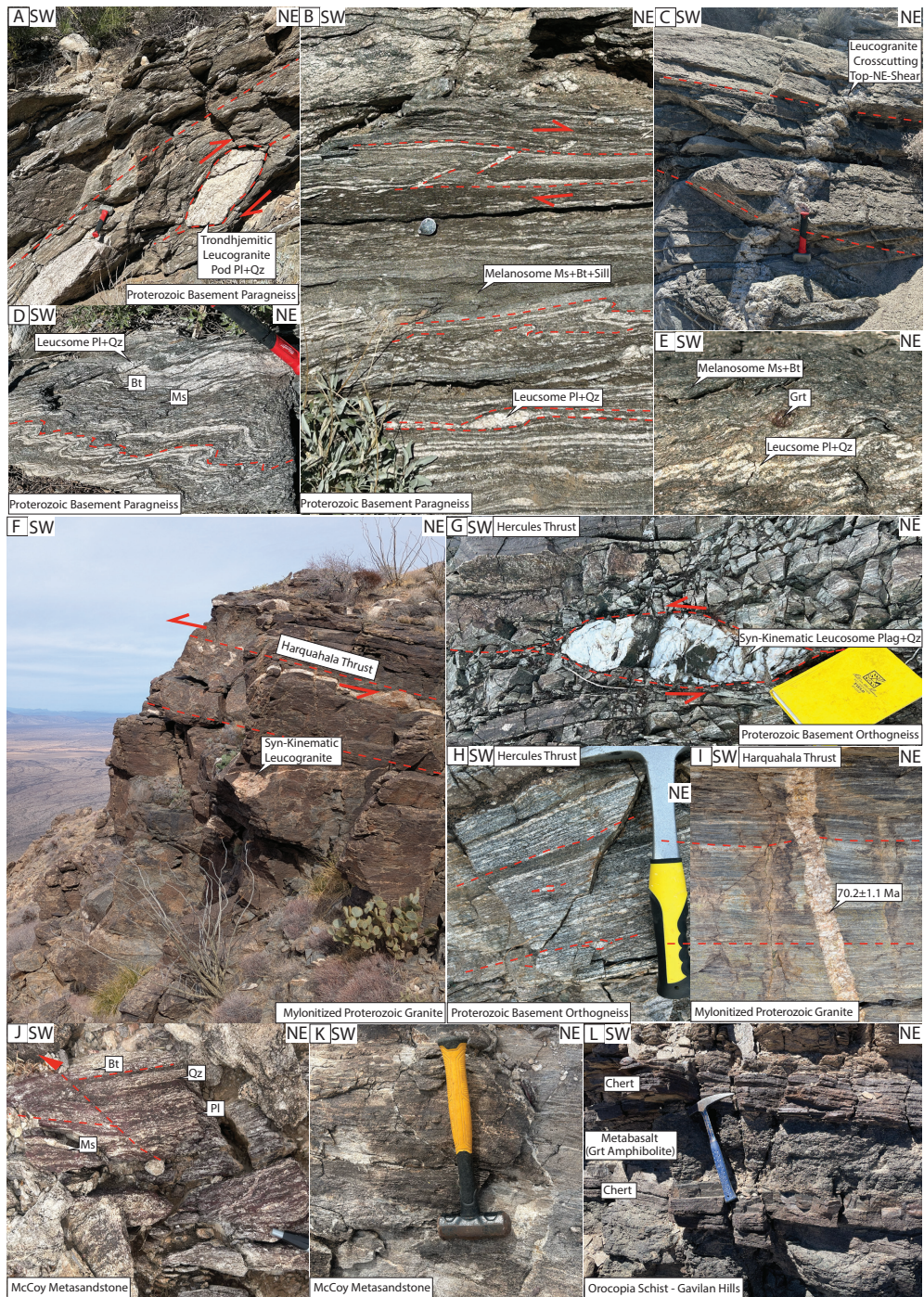


Fig. 5: Field photographs showing the main cross-cutting relationships of the Harcuvar, Harquahala and Granite Wash Mts. In particular top-NE shear occurred in the presence of partial melt at high structural levels, whereas top-SW shearing occurred at deeper structural levels, note the decreasing metamorphic grade with increasing structural depth. A-B) Top-NE shearing affecting anatectic features including leucosomes and leucogranite pods in the Harcuvar Mts. C) NNE-SSW trending steeply dipping leucogranite pegmatite dyke cross-cutting the top-NE shear fabrics. D-F) Leucosomes folded with a NE-trending vergence and shallow plunging NE-trending hinge lines. F) Syn-kinematic leucosomes and leucogranites aligned along the Harquahala Thrust. G) Asymmetric leucosome porphyroclast with top-SW shear sense, H) Mylonitized Proterozoic orthogneiss from the Hercules Thrust. I) Sample 25-24 leucogranite vein, cross-cutting the top-SW mylonite fabric on the Harquahala Thrust. J-K) Deformed greenschist facies Late Cretaceous McCoy metasediments in the footwall of the Hercules Thrust. L) Garnet Amphibolite mafic schist intercalated with metachert representing Farallon Plate ocean plate stratigraphy, from the Orocopia Schist in the Gavilan Hills.

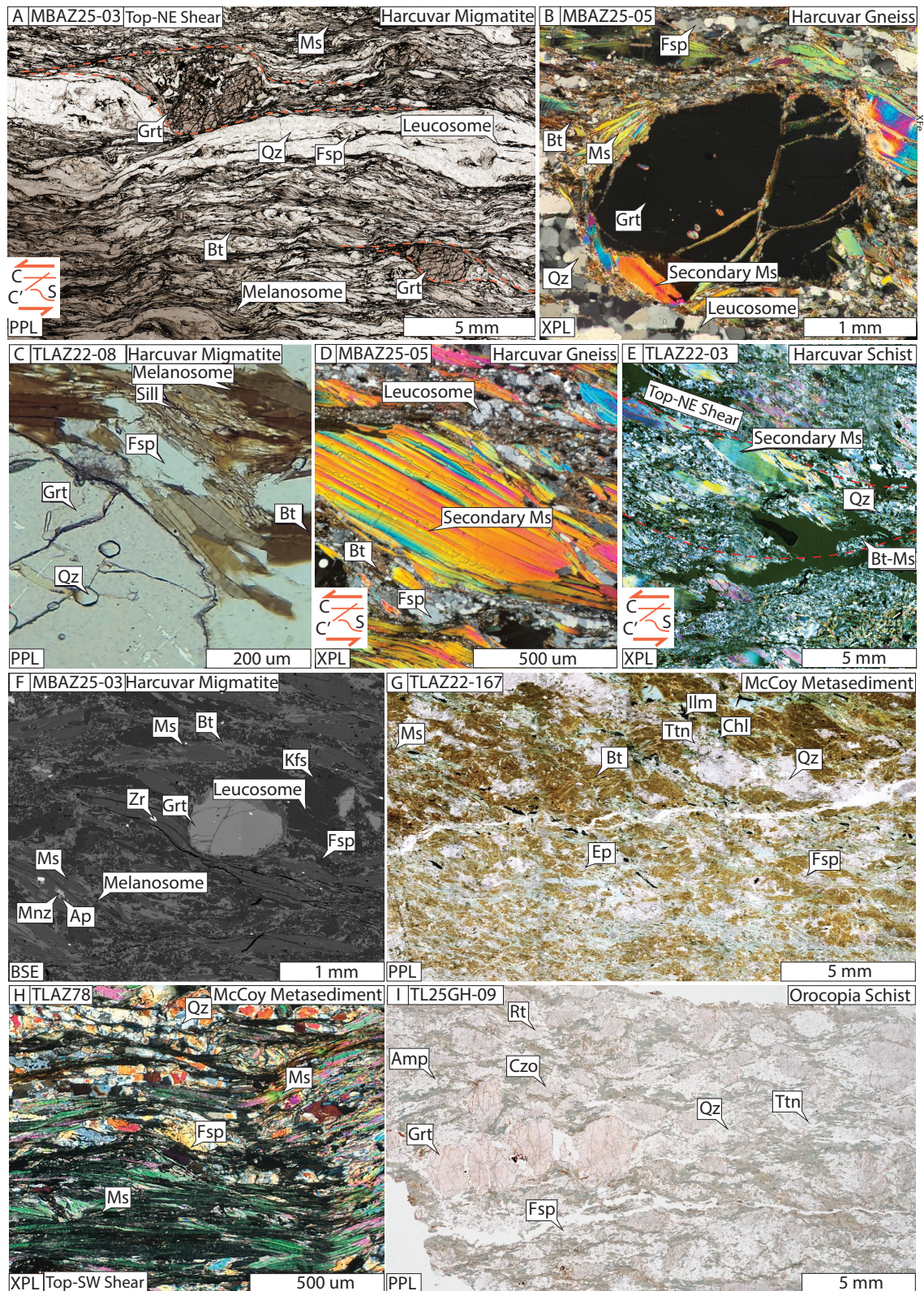
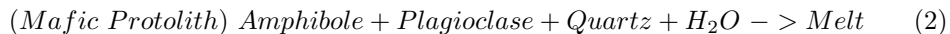
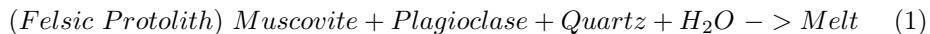


Fig. 6: Photomicrographs documenting petrography of A-E) Sillimanite migmatite in hanging wall of the Hercules Thrust, G-H) Greenschist facies McCoy metasediment in the footwall of the Hercules Thrust and I) Sample TL25GH-09, a garnet amphibolite from the Orocopia Schist at the Gavilan Hills.

241 are affected by intense mylonitization and locally partial melting. Shear sense indi-
 242 cators including sigma porphyroclasts and deformed leucosomes also show top-SW
 243 asymmetry, whereas some leucocratic veins and dykes cross-cut the foliation, clearly
 244 indicating that thrusting was coeval with anatectic conditions. Leucogranitic dike sam-
 245 ple 25-24 which cross-cuts the mylonitic foliation in the footwall (Fig. 5I) yielded a
 246 zircon $^{238}\text{U}/^{206}\text{Pb}$ weighted mean age of 70.2 ± 1.1 Ma, suggesting top-SW thrusting
 247 ended by this time. Two additional samples, from the hanging wall (sample 25-05)
 248 and footwall (sample 25-14) of the Harquahala Thrust yield zircon U-Pb discordia
 249 lower intercept ages of 119 ± 53 Ma, and 73 ± 24 Ma respectively, which overlap with
 250 the weighted mean age of the cross-cutting dike. These ages also overlap with unpub-
 251 lished U-Pb titanite geochronology from shear zones with top-SW kinematics in the
 252 hanging wall between ca. 76-69 Ma (Pollard, 2014). Together, these data suggest that
 253 upper amphibolite facies metamorphism and movement along the Harquahala Thrust
 254 occurred at ca. 70 Ma.

255 Moving up structural section, in the hanging wall of the Harquahala Thrust near
 256 Brown's Canyon in the northeastern Harquahala Mountains, the abundance of leu-
 257 cosomes increases and some rocks show garnet and kyanite or sillimanite bearing
 258 mineral assemblages, that are pre-syn tectonic with respect to the foliation, indicating
 259 an inverted metamorphic field gradient. Along this section, the kinematic indicators
 260 also reverse to top-NE directed shear. Top-NE shearing also affects the peraluminous
 261 Brown Canyon granite dated at ca. 75 Ma (Pollard et al., 2014; Isachsen et al. 1999).
 262 Similar field relationships also occur in the Harcuvar Mountains, as migmatites and
 263 leucogranites crop out within Proterozoic basement protoliths to the NE of the ca.
 264 74-64 Ma Tank Pass Granite (Wong et al. 2023).

265 Approximately 8 km above the Hercules Thrust in the Harcuvar Mountains, volu-
 266 metrically abundant (locally $>35\%$ rock volume) leucosomes occur within paragneiss
 267 and amphibolite. The leucosomes have trondhjemitic (plagioclase-quartz) composi-
 268 tions and show diffuse boundaries (Figs. 5A-E and 6A). There is also minor ($<1\%$)
 269 kyanite or sillimanite (Fig. 6C), and negligible peritectic k-feldspar (Fig. 6F) yet abun-
 270 dant secondary muscovite and biotite that occurs as mm-cm sized flakes (Fig. 6D-E).
 271 These observations are inconsistent with the migmatite petrogenesis being a product
 272 of muscovite dehydration melting above the solidus. This is because, during muscovite
 273 dehydration melting, k-feldspar, sillimanite and melt should have a stoichiometric
 274 ratio of 8/5/10 (Dyck et al. 2020). Furthermore, the trondhjemitic leucosome com-
 275 positions and secondary muscovite implies that anatexis occurred by the addition of
 276 water, and resulted in the breakdown of plagioclase and k-feldspar (reaction 1 for a
 277 felsic protolith and reaction 2 for a mafic protolith).



280 Many of the leucosomes are ptlygmatically folded with a NE-directed vergence, have
281 sub-horizontal NE-trending hinge lines, and are sheared with top-NE/ENE kinematic
282 indicators. Millimetric to centimetric sized flakes of secondary muscovite, that likely
283 grew during melt crystallization, also show top-NE asymmetries, suggesting ductile
284 shearing continued during cooling through the water-saturated solidus. All these fea-
285 tures are consistent with partial melting occurring by the addition of water (Weinberg
286 & Hasalova, 2015) during exhumation within a NE-dipping 'extensional' shear zone.

287 A sillimanite bearing migmatite (sample TLAZ22-08) and schist (TLAZ22-02) from
288 the Central Harcuvar Mountains yielded U-(Th)-Pb monazite dates of ca. 76-58 Ma
289 with elevated Gd/Yb ratios between ca. 73-60 Ma (Fig. 7), likely recording monazite
290 growth in the presence of garnet (Spear & Pyle, 2002, 2010). Sample TLAZ22-08
291 records peak metamorphic conditions of 0.75 ± 0.08 GPa and $777 \pm 36^\circ\text{C}$, which
292 were calculated from garnet core compositions in equilibrium with biotite-sillimanite-
293 plagioclase-quartz and minimal k-feldspar, whereas the garnet outer rim records 0.59
294 ± 0.08 GPa and $754 \pm 24^\circ\text{C}$ implying decompression above the solidus (Lamont et al.
295 2024; Fig. 8). Walsh et al. (2016) also reported U-(Th)-Pb monazite dates from the
296 Harcuvar mountains between ca. 76-70 Ma and argue for a decompression P-T path
297 from ca. 1.0-0.6 GPa, related to retrograde staurolite growth. U-Pb geochronology of
298 syn-tectonic titanite within top-NE shear zones in the Harquahala Mountains gave
299 dates between ca. 72-68 Ma (Pollard et al. 2014).

300 However, the top-NE shear fabrics and migmatite features are cross-cut by NNE-
301 SSW and NNW-SSE trending Ms+Grt±Bt leucogranite and pegmatite dykes that
302 have been dated between ca. 70-55 Ma (Isachsen et al. 1999; Wong et al. 2023; Fig. 5C).
303 Integrating these data implies that high temperature top-NE shearing occurred before
304 Miocene extension and in the presence of partial melt and during the decompression
305 of rock between ca. 76-63 Ma.

306 During this same time interval, the Pelona-Orocopia-Rand Schists (PORS),
307 exposed in the nearby Plomosa mountains, Cemetery Ridge and the Gavilan Hills in
308 SE California (Figs. 2 and 4) were underplated directly beneath the base of the North
309 American crust as a result of low angle subduction of the Farallon Plate between ca.
310 70-65 Ma (e.g. Chapman, 2018; Strickland et al., 2018; Haxel et al. 2022). A sample of
311 garnet amphibolite (TL25GH-09) intercalated with metachert that represents a frag-
312 ment of oceanic plate stratigraphy enclosed within the metasedimentary schist at the
313 Gavilan Hills records prograde metamorphic garnet zonation associated with a convex-
314 down zoning profile of Mn from core to rim whereas both Ca and Mg increase over the
315 same interval (supplementary material). Chemical compositions of garnet core and rim
316 in equilibrium with amphibole, plagioclase, quartz, epidote, rutile, ilmenite and titan-
317 ite, indicate that garnet grew on a clockwise prograde P-T path from 0.7 ± 0.05 GPa
318 and $554 \pm 15^\circ\text{C}$ and to peak P-T conditions of 0.8 ± 0.09 GPa and $592 \pm 39^\circ\text{C}$. U-Pb
319 zircon geochronology constrains peak metamorphism between ca. 70-65 Ma (Haxel et
320 al., 2022; Jacobson et al. 2007). In contrast, detrital zircon analysis from these rocks
321 suggest they were deposited at the trench at ca. 73 Ma (Seymour et al. 2018; Jacobson
322 et al. 2007). Since PORS is also exposed in the Plomosa Mts (Strickland et al. 2016;

323 ~25 km away from the Harcuvar Mountains), the similar peak pressures and overlap-
324 ping timing of metamorphism of the PORs and the Harcuvar-Harquahala migmatites
325 requires an explanation, which we discuss below.

326 DISCUSSION

327 A Case for Channel Flow in Arizona

328 The new field observations, thermobarometry and geochronology, demonstrate that
329 an inverted metamorphic field gradient occurs across the Hercules, Centennial and
330 Harquahala Thrusts and moving further northeast up structural section across the
331 Harquahala and Harcuvar Mountains. These structures were responsible for over-
332 thrusting metamorphosed Proterozoic basement towards the SW onto Cretaceous
333 sediments and Jurassic volcanics. Top-SW shearing likely commenced in the region
334 at ca. 86 Ma as the Tyson Wash granite in the northern Dome Rock Mountains was
335 syn-to-post kinematic with respect to the Tyson-Valenzuela thrust (Boettcher, 1996;
336 Isachsen et al., 1999) and shearing was ongoing on the Hercules, Centennial and Har-
337 quahala Thrusts between ca. 76-70 Ma (Fig. 7). In contrast above the thrusts, at
338 higher structural levels, higher grade metamorphic rocks, migmatites and leucogran-
339 ites are affected by opposite top-NE shearing that pre-dated the Miocene extension
340 as the fabrics are cross-cut by ca. 63-55 Ma undeformed pegmatites and leucogranite
341 dikes (Wong et al. 2023).

342 Top-NE shearing is associated with normal sense displacement and outcrop fab-
343 rics and structures suggest it occurred in the presence of partial melt between ca.
344 76-63 Ma (Fig. 7). Therefore, both shear zones with opposite kinematics were active
345 at the same time approximately between ca. 76-70 Ma (Fig. 7). The field relations
346 and P-T-t data also require that the thrust responsible for the burial and prograde
347 metamorphism of the gneisses and migmatites within the overthrust sheets to peak
348 metamorphic pressures of 0.75 GPa (~28-30 km depth) was not the Hercules, Centen-
349 nial or Harquahala Thrusts. It must have been a structurally higher thrust that was
350 active earlier and potentially reactivated with top-NE kinematics.

351 Because the Mesozoic metasedimentary rocks structurally beneath the Hercules
352 Thrusts never achieved pressures greater than ~0.4 GPa, it requires that the over-
353 thrust sheet of high-grade metamorphic rocks once buried at ~28-30 km depth (as
354 implied by the metamorphic pressures of 0.75 GPa) was extensively thinned at the
355 same time as overthrusting. If no thinning of the overthrust sheet occurred, meta-
356 morphic pressures in the immediate footwall of the Hercules Thrust should be greater
357 than 0.75 GPa (Fig. 8). Rapid erosion (>2 km/Myr) could potentially explain this
358 data, however one would expect to see a significant amount of detrital metamor-
359 phic grains within the McCoy Mountains Formation. Furthermore, rapid erosion alone
360 cannot explain the opposing high temperature kinematic indicators.

361 Our preferred interpretation to rectify the field observations and P-T-t data is the
362 operation of a syn-orogenic extrusion mechanism (channel flow) that transported weak
363 partially melted mid to lower crust towards the SW (Fig. 9). In this model, the Hercules
364 Thrust associated with top-SW kinematics would define the base of the extruding

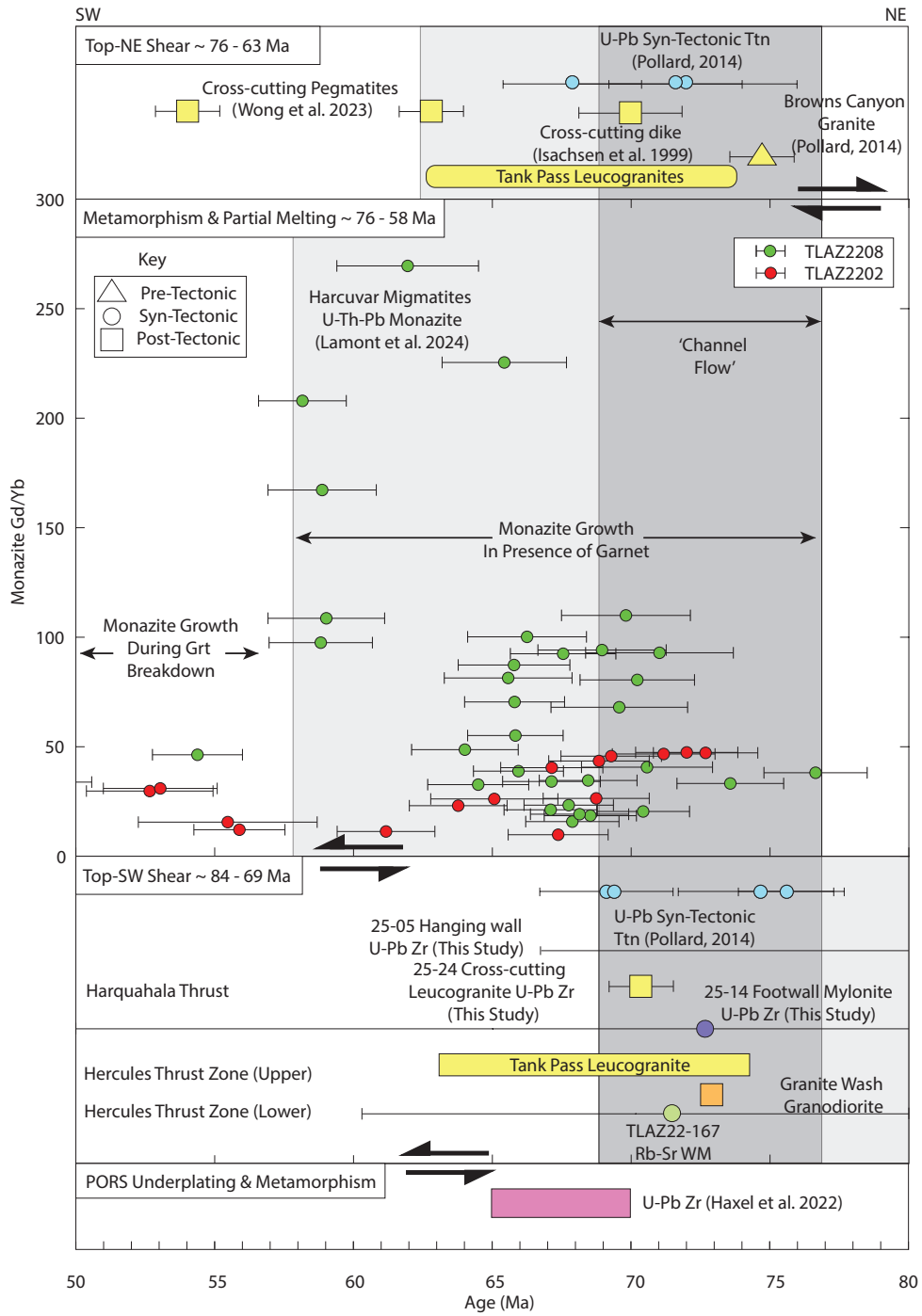


Fig. 7: Time chart showing the overlapping timing constraints for metamorphism and partial melting, top-SW shearing and top-NE shearing

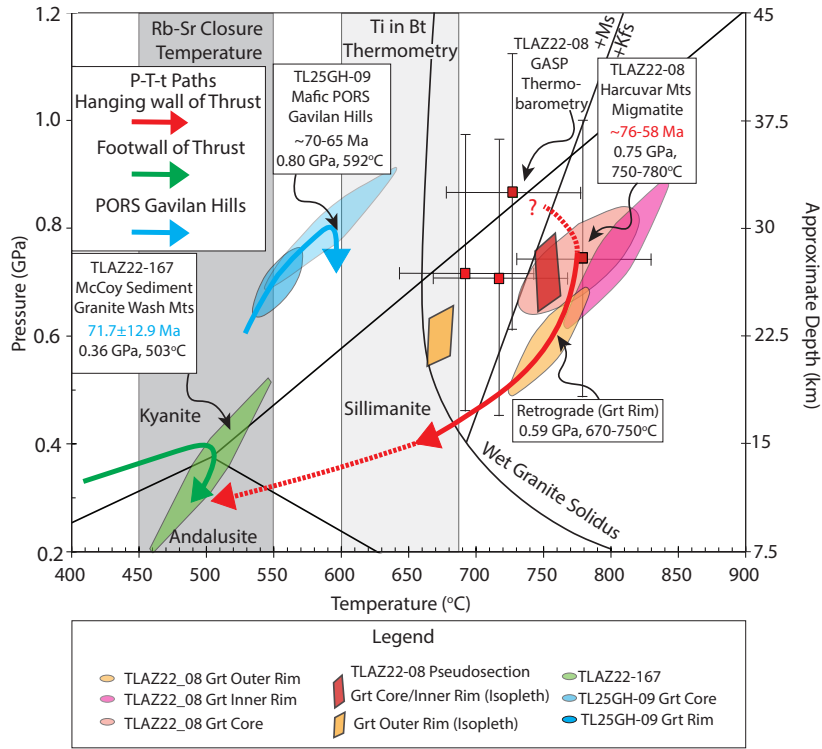


Fig. 8: P-T-t diagrams highlighting the calculated P-T conditions for TLAZ22-167, TLAZ22-08, and TLGH25-09. Note the contrasting P-T loops in the hanging wall and footwall of the Hercules Thrust and the underplated Pelona-Orocopia-Rand-Schists (PORS), integrated with geochronology. Also note the similar peak pressures in the hanging wall migmatites and PORS.

365 channel or wedge of high-grade metamorphic rocks and migmatites, whereas the top-
 366 NE shear zones within the migmatites at higher structural levels would represent a
 367 passive roof normal fault defining the top of the channel. Since both top-SW and
 368 top-NE shear zones were active simultaneously between ca. 76-70 Ma, syn-orogenic
 369 extrusion or channel flow can therefore explain the exhumation of rock from pressures
 370 of ca. 0.75-0.36 GPa, without burying the footwall to significant depths.

371 At approximately this same time interval (ca. 70-65 Ma), the PORS were under-
 372 plated directly beneath the North American crust and record similar pressures of ca.
 373 0.8 GPa to that of the migmatites within the overthrust sheets (Fig. 8). The overlap-
 374 ping metamorphic pressures, timing of metamorphism, and proximity of the PORS to
 375 the Harcuvar-Harquahala migmatites (~25 km), therefore potentially creates a space
 376 problem if there was no differential movement of mid to lower crustal material (Fig.
 377 9B).

378 However, volatiles released from dehydration reactions occurring along the low-
 379 angle Farallon plate interface likely migrated directly across the Moho and into the

380 base of the overlying North American crust (Lamont et al. 2024). The addition of slab
381 derived volatiles (e.g. H₂O, CO₂) would act to reduce the solidus of previously dry
382 Proterozoic aged mid to lower crustal rocks and cause significant water-fluxed crustal
383 melting (reaching up to 35% volume locally). This magnitude of partial melting would
384 cause a breakdown in the solid rock framework (Rosenberg & Handy, 2005; Jamieson et
385 al. 2011). This would cause significant rheological weakening, and a viscosity reduction
386 by up to four orders of magnitude (from $\sim 10^{21}$ to $\sim 10^{17}$ PaS), resulting in significant
387 lateral and vertical density contrasts within the North American crust. Additionally,
388 because the Colorado Plateau to the immediate NE of the area remained relatively
389 undeformed during the Sevier-Laramide orogenies and subsequent Cenozoic extension,
390 and maintained >100 km lithospheric thickness (Golos & Fischer, 2022), it likely
391 acted as a rigid backstop, buttressing the Late Cretaceous contractional deformation.
392 It is also possible that the focused contraction caused the lower crust to be initially
393 underthrust beneath the lithospheric wedge at the western margin of the Colorado
394 Plateau. This would be consistent with the thick crust (>50 km) along the Colorado
395 Plateau Transition Zone that is predicted in palithspathic restorations (Bahadori et
396 al. 2018). The combination of these processes potentially facilitated ductile extrusion
397 of the mid to lower crust towards the SW. This extrusion mechanism is also consistent
398 with the pulse of uplift along the Colorado Plateau Transition Zone (Kapp et al. 2023),
399 associated with bulldozing the lower crust and subcontinental lithospheric mantle
400 during the onset of low angle subduction (Chapman et al. 2020; Kapp et al. 2023).

401 Underplating a significant thickness of the PORs, (likely >8 km constrained by
402 seismic reflection investigations beneath the Mojave; Cheadle et al. 1986) also added
403 buoyant felsic meta-sedimentary material to the base of the North American crust
404 in place of lithospheric mantle. This likely caused isostatic uplift and increased grav-
405 itational potential energy above the area of underplating and flat slab subduction.
406 However, the area was likely still in an overall contractional setting due to strong
407 coupling along the plate interface, bulldozing the sub-continental lithospheric mantle
408 and end-load at the trench. However, on longer timescales, continued underthrust-
409 ing of the Farallon flat slab caused cooling and refrigeration of the North American
410 crust (English et al. 2003), consistent with peak metamorphism lasting only ~ 10 -15
411 Myrs and followed by cooling between ca. 60-40 Ma, constrained by Rb-Sr and Ar-Ar
412 cooling ages from the region (Richard et al. 1990; Lamont et al. 2024).

413 Although the P-T-t data we present and discuss here from the Harcuvar, Harqua-
414 hala and Granite Wash Mountains is fairly limited, it is consistent with the 1st order
415 predictions of syn-convergent extrusion or channel flow. However, further structural,
416 geochronological and petrological investigations on these rocks will lead to a much
417 greater understanding and rigorously test our proposed model.

418 **Implications for Cordilleran Tectonics**

419 Although the mid to lower crust is rarely exposed across the SW USA in such a
420 complete section, there are numerous magnetite bearing Ms+Grt \pm Bt peraluminous
421 intrusions that have isotopic and petrological features consistent with water-fluxed
422 melting of Proterozoic crust, as recorded in the Harcuvar-Harquahala migmatites.
423 Water-fluxed crustal melting preferentially consumes plagioclase and K-feldspar which

424 are the main hosts of Sr in a rock. Therefore, water-fluxed crustal melting would be
425 expected to produce a hydrous, siliceous and oxidized melt that has an elevated Sr/Y
426 ratio. Such magmas are consistent with the petrography and geochemistry of many
427 peraluminous granites across Arizona and the SW USA.

428 Metaluminous and peraluminous intrusions and porphyry copper deposits get sys-
429 tematically younger across Arizona from NW to SE between ca. 73-45 Ma. From
430 NW-SE the peraluminous intrusions include Diamond Joe (ca. 72 Ma; Chapman et
431 al. 2017), Tank Pass Granite (ca. 75-66 Ma; Isachen et al. 1999; Wong et al. 2023),
432 Vulture Mountains (ca. 68 Ma; Rehrig et al. 1980); White Tank Mountains (ca. 56
433 Ma; Lamont et al. 2024), Pichacho Mts (ca. 58 Ma), Wilderness Suite Granite (ca.
434 56-45 Ma; Fornash et al. 2013) in the Catalina-Rincon MCC, Pan Tak granite (58-
435 48 Ma; Chapman et al. 2023) in the Coyote Mts, Texas Canyon (56 Ma; Lamont et
436 al. 2024) in the Dragoon Mountains, and the Renello Suite Granites in the Pinaleño
437 Mountains (ca. 56 Ma; Scoggin et al. 2021). The diachronous timing of these crustal-
438 derived granites implies a mid-crustal zone of water-fluxed partial melting that also
439 systematically gets younger towards the SE during the Late Cretaceous to Paleocene.

440 Water-fluxed crustal melting in Arizona can be explained by the addition of water
441 derived from metamorphic dehydration reactions that occurred on the Farallon slab
442 infiltrating directly across the Moho, during the onset of low angle subduction, before
443 significant refrigeration occurred (Lamont et al. 2024). Therefore, the southeastward
444 migration of water-fluxed crustal melting likely corresponds to time transgressive
445 Farallon slab-flattening (Lamont et al. 2024).

446 An additional noteworthy observation is that, upon restoring the Miocene exten-
447 sion, the Harcuvar and Harquahala migmatites dated at ca. 76-60 Ma would project 60
448 km towards the NE, directly beneath the ca. 72 Ma Bagdad porphyry copper deposit
449 (Barra et al. 2003). Therefore the mid to lower crustal exposures of migmatites and
450 anatectic rocks may represent the deep crustal root zone of the Laramide porphyry
451 copper deposits.

452 However, there is only relatively local evidence of this ductile extrusion process
453 confined to the MFTB and eastern Mojave Desert. Several Late Cretaceous extensional
454 shear zones are exposed across the Mojave region (Hodges & Walker, 1992; Wells
455 & Hoisch, 2008) which could represent the roof shear zone of an extruding channel.
456 In particular, the Little Piute Mountains, Old Woman Mountains and the Kilbeck
457 Hills in SE California, expose the E verging Scanalon Thrust and W verging Meteor
458 Fault, which are parallel structures separated by 1-2 structural km and show opposing
459 kinematics (Howard et al. 1997). These structures have been previously interpreted
460 as forming during a phase of contraction followed by regional extension at ca. 73 Ma
461 (Hodges and Walker, 1992; Wells & Hoisch, 2008). Alternatively, it may be possible
462 that these structures represent the continuation of a westward verging syn-orogenic
463 mid-crustal channel of high-grade metamorphic rock.

464 However, elsewhere in southern Arizona, where crustal melts and peraluminous
465 granites are exposed, there is only limited evidence for syn-anatectic thrusting. The
466 best example is a thrust fault which mylonitizes the roof of the ca. 56 Ma Texas
467 Canyon Ms+Bt+Grt peraluminous granite in Dragoon mountains in SE Arizona.

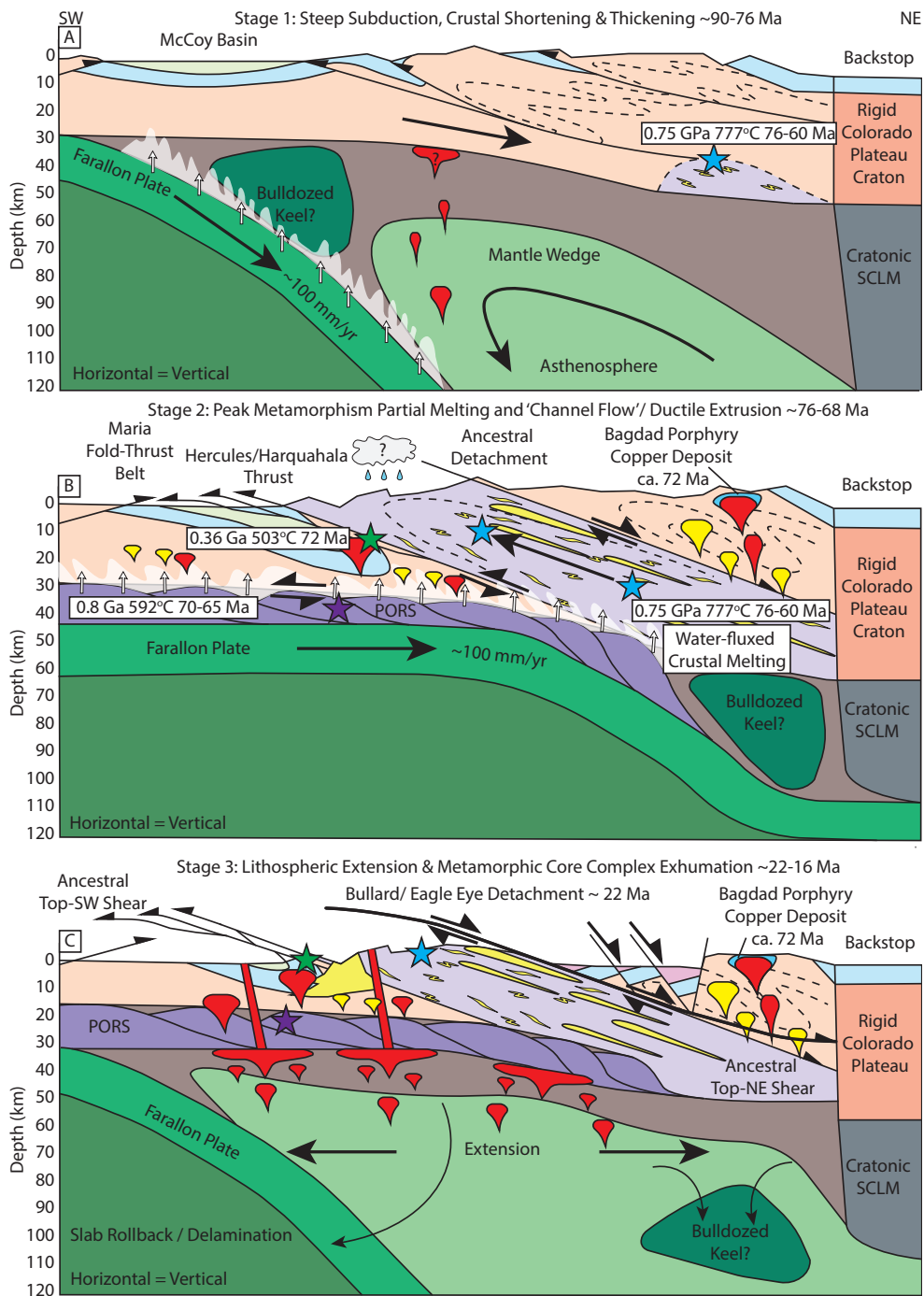


Fig. 9: Channel Flow Model for the Harcurvar-Harquahala-Granite Wash Mountains. A) Stage 1: Contraction and crustal thickening resulting in burial of rocks and heating during steep subduction of the Farallon Plate between ca. 90-76 Ma. B) Stage 2: Onset of low angle subduction resulting in underplating of the PORC at 0.8 GPa, resulting in dehydration reactions liberating fluid and inducing water-fluxed crustal melting and rheological weakening of the mid to lower North American Crust, resulting in ductile extrusion of the mid to lower crust towards the SW, i.e. 'channel flow' between ca. 76-68 Ma forming the ancestral top-SW shear fabrics along the channel base and top-NE shear fabrics along the channel passive roof shear zones. C) Stage 3: Slab delamination and onset of Miocene regional extension forming the Bullard and Eagle Eye Detachments that reactivate and capture the earlier extrusion related shear zones.

468 Here, the Pinal Schist Proterozoic basement is thrust on top of Cretaceous Bis-
469 bee group sediments and the thrust is cut by a Grt+Ms pegmatite dike (personal
470 observation; Keith et al. 2025) suggesting thrusting during the early stages of plu-
471 ton emplacement. However, the extensive peraluminous crustal derived granites in the
472 Catalina-Rincon MCC, Coyote, Pinalaño Mountains do not appear to be bound by
473 thrust faults, and the timing of thrusting in these areas is interpreted to be 75-65 Ma
474 (e.g. Favorito & Seedorf, 2024), which is \sim 10-15 million years before the emplacement
475 of the peraluminous anatectic rocks. The ductile extrusion feature we document in the
476 Harcuvar-Harquahala-Granite Wash mountains is therefore unlikely to be an orogen
477 wide structure.

478 Finally, our proposed syn-orogenic extrusion mechanism during the underplating
479 and accretion of the PORS could explain the paradoxical geochemical and metamor-
480 phic evidence for thick crust across Arizona during the Late Cretaceous-Paleocene
481 (Chapman et al. 2020; Lamont et al. 2024) and the relatively scarce evidence for upper-
482 crustal shortening features as the crust was thickened from primarily underplating.
483 Syn-orogenic extrusion may also facilitate the localization of extensional strain and
484 final MCC exhumation in the same location during delamination of a low angle slab
485 at a later time.

486 **Comparison with the Himalaya and East Greenland** 487 **Caledonides**

488 Closer inspection of the Harcuvar-Harquahala-Granite Wash Mountains reveals many
489 similarities, and a few key differences with the Greater Himalayan Series (GHS) and
490 the retro-wedge of the East Greenland Caledonides (EGC) (Fig. 10).

491 All three locations show inverted metamorphic isograds along the basal thrust
492 fault (Main Central Thrust at the base of the GHS, a thrust fault separating the fore-
493 land and 'infrastructure' in the EGC, and the Hercules/Harquahala Thrusts at the
494 base of the Harcuvar-Harquahala migmatites in Arizona; Fig. 10). These inverted iso-
495 grads can be spatially linked with right-way up metamorphic isograds associated with
496 opposing normal sensed shear at higher structural levels along the channel ('infras-
497 tructure') roof (Searle and Rex, 1989, Hodges, 2016). Thermobarometric data support
498 this interpretation, as P-T conditions increase up-section above the Hercules and Har-
499 quahala Thrusts in the Harcuvar, Harquahala and Granite Wash Mountains from
500 greenschist to upper amphibolite facies (0.36 Ga and 503°C to 0.75 GPa and 777°C),
501 similar to structurally above the Main Central Thrust in the Himalaya and above the
502 base of the EGC 'infrastructure' (White and Hodges, 2002), although in some places
503 the thrust has been reactivated as an extensional detachment (Hodges, 2016). In con-
504 trast, supra-solidus deformation is overprinted by sub-solidus deformation beneath the
505 South Tibetan Detachment (STD), Fjord Region Detachment (FRD) and the Late
506 Cretaceous-Paleocene syn-migmatitic mylonites in the Harcuvar-Harquahala Moun-
507 tains. The highest-grade rocks therefore appear close to the center to upper half of
508 the GHS, EGC 'infrastructure' and the Harcuvar-Harquahala MCCs.

509 Leucogranites are also abundant in all three settings and are spatially related
510 to a widespread sillimanite-bearing migmatite zone and consist of multiple phases
511 of intrusions spanning \sim 10 Myrs (Searle et al. 2010; Wong et al. 2023). The

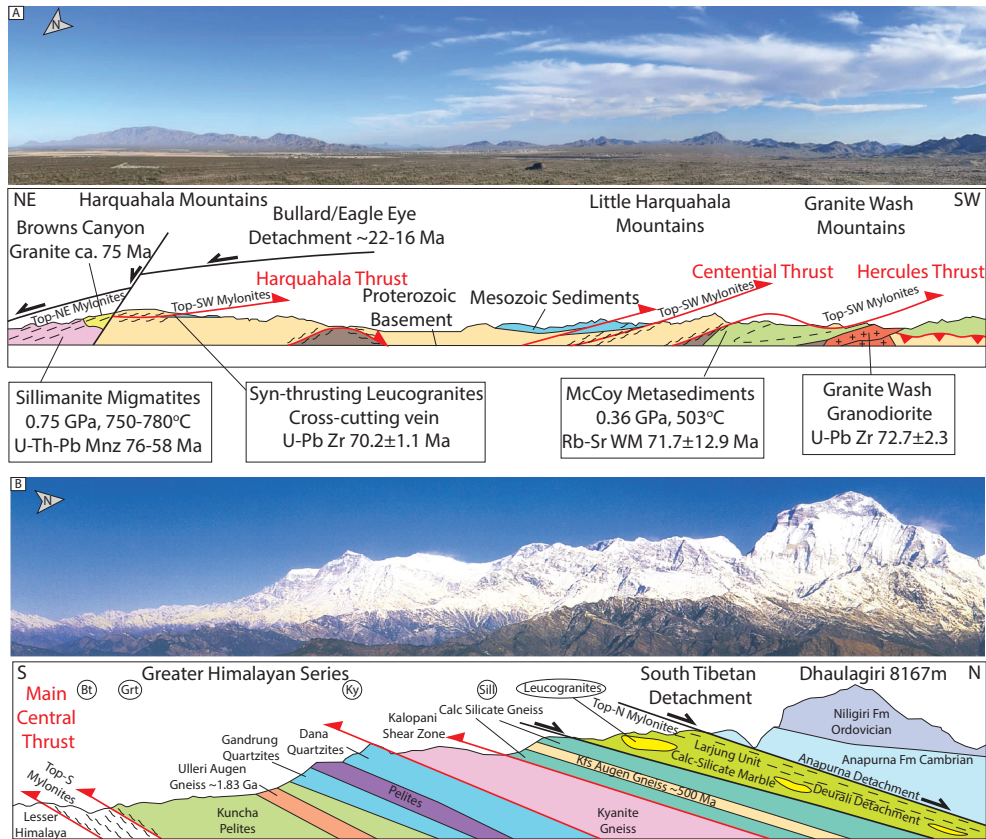


Fig. 10: Comparison between the field relationships and metamorphism in A) the Harcuvar-Harquahala-Granite Wash Mountains and B) the Greater Himalayan series in the high Himalaya adapted from Searle, (2010).

512 leucogranites in the Himalaya and Arizona have the composition quartz–K-
 513 feldspar–plagioclase–muscovite–tourmaline–biotite–garnet, with some later intrusions
 514 containing magmatic cordierite (altered to pinite) and/or andalusite. The leucogran-
 515 ites are also highly peraluminous (molar A/CNK > 1.1), contain high boron
 516 concentrations (abundant tourmaline), and elevated $^{87}\text{Sr}/^{86}\text{Sr}$ ratios, indicating a
 517 purely crustal melting origin (Harris & Massey 1994; Hopkinson et al. 2020; Lamont
 518 et al. 2024).

519 However, the ca. 74-64 Ma Tank Pass leucogranite in the Harcuvar and Granite
 520 Wash Mountains cross-cut top-SW shear fabrics, whereas ca. 70-55 Ma pegmatitic
 521 dikes cross-cut top-NE shear fabrics. This is somewhat similar to the anatectic granites
 522 of the infrastructure in EGC (Hodges et al. 2016), where unfoliated late-stage anatectic
 523 melts cut FRD fabrics and in some cases intrude across the FRD and into the overlying
 524 'superstructure', effectively constraining the age of the FRD to ca. 425 Ma (White et
 525 al. 2002).

526 U–(Th)–Pb monazite dating shows that peak metamorphism and melting in the
527 GHS evolved from late Eocene–Oligocene kyanite-grade metamorphism to lower pres-
528 sure and higher temperature sillimanite-grade metamorphism. During the later stages
529 cordierite formed at pressures <0.5 GPa. Kyanite grade partial melting is repre-
530 sented by small, plagioclase-poor, kyanite+quartz-bearing leucosomes within the GHS
531 gneisses. These melts formed at $\sim 720\text{--}710^\circ\text{C}$ and ca. 1.0 GPa by water-fluxed melting
532 between ca. 40–30 Ma (Laccarino et al. 2015). However, most GHS leucogranites were
533 formed by muscovite or biotite dehydration reactions due to decompression between
534 ca. 25–15 Ma (Cottle et al. 2009, 2015). Mid-crustal melting during the early to mid-
535 Miocene likely triggered the large-scale ductile flow of a partially molten layer of
536 mid-crust bounded by the MCT ductile shear zone below and the STD ductile shear
537 zone and low-angle normal faults above.

538 Within the the EGC ‘infrastructure’, metamorphic conditions reached upper
539 amphibolite to granulite facies with extensive partial melting during Caledonian defor-
540 mation (ca. 440–405 Ma) which overlaps with the timing of normal sensed shearing
541 on the roof shear zone (ca. 440–425 Ma) (Andresen et al. 2007; Elvevold et al. 2003;
542 Gilotti & McClelland 2005; Hartz et al. 2000, 2001; Kalsbeek et al. 2001; Strachan &
543 Martin 2001; Watt et al. 2000; White & Hodges 2003; White et al. 2002).

544 Migmatites from the Harcuvar Mountains give U–(Th)–Pb monazite dates span-
545 ning ca. 76–58 Ma (Walsh et al. 2016; Lamont et al. 2024) that represent the timing
546 of peak metamorphism and crustal anatexis that overlap with the timing of top-SW
547 thrusting (ca. 86–70 Ma) and top-NE shearing (ca. 76–63 Ma). The migmatites also
548 record a similar P–T path to the GHS with kyanite overprinted by sillimanite asso-
549 ciated with decompression and partial exhumation. However, Harcuvar-Harquahala
550 migmatites have very extensive leucosome components locally comprising >30–35% of
551 the rock volume, and they have trondhjemitic (plagioclase-quartz) compositions. There
552 is also minimal peritectic K-feldspar yet abundant muscovite in partially melted Pro-
553 toerozoic gneisses. Together, these features suggest that partial melting occurred by the
554 addition of water, which preferentially consumed plagioclase during anatexis (Lamont
555 et al. 2024), rather than incongruent melting of muscovite or biotite (Weinberg and
556 Hasalova, 2015). Since plagioclase is the main host of Sr, water-fluxed crustal melting
557 can potentially explain the high Sr/Y ratios that characterize the Late-Cretaceous-
558 Paleocene peraluminous granites across Arizona and the SW USA (Chapman et al.
559 2020).

560 However, water-fluxed crustal melting requires an external source of water. In Ari-
561 zona, this was likely derived from dehydration reactions occurring within the upper
562 part of the low angle Farallon slab, based on the overlapping timing of metamorphism
563 (ca. 70–65 Ma) recorded by the PORS. In contrast, the age of PORS underplating,
564 water-fluxed crustal melting, and peraluminous granite intrusion is older to the west
565 in the Mojave Desert, implying the locus of slab dehydration and water-fluxed crustal
566 melting was time transgressive and was followed by refrigeration due to progressive
567 underplating. In contrast, the deep crustal earthquakes within the Indian shield under-
568 thrusting beneath the Himalaya suggest it consists of dry granulites that have been
569 previously dehydrated (Priestley et al. 2008), and therefore an unlikely source of water.

570 As such, most Himalayan migmatites and leucogranites formed by the incongruent
571 breakdown of muscovite (e.g. Patiño Douce & Harris, 1998).

572 The Harcuvar-Harquahala-Granite Wash Mountains and the EGC retro-wedge also
573 show along strike variation in metamorphic grade, and diachronous timing of thrusting
574 and ductile flow within the mid to lower crustal channel ('infrastructure') (Hodges,
575 2016), which contrasts with the Himalaya. Both settings are also affected by post-
576 orogenic regional extension (McClay, 1986), that in some cases reactivates the earlier
577 shear zones (Hodges, 2016). In Arizona, regional extension occurred at ca. 22-16 Ma,
578 whereas within the EGC it occurred at ca. 350-360 Ma. In both settings, regional
579 extension commenced some ca. 40-50 Myrs after a phase of syn-convergent extrusion.

580 In summary, all three locations show a similar overall trans-lithospheric orogenic
581 structure separated by key decoupling horizons (Hodges, 2016): 1) An 'extensional'
582 decoupling horizon representing the strain discontinuity existing between the upper
583 crustal 'superstructure' and mid to lower crustal 'infrastructure', associated with exci-
584 sion of crust through large-displacement normal faulting. Although this decoupling
585 horizon may be referred to as an extensional fault because of the kinematics, it does not
586 indicate extension on the scale of the entire crust because the upper crustal extension
587 is compensated for by contractional deformation at deeper structural levels (Hodges,
588 2016). 2) The base of the channel or 'infrastructure' represents large-displacement
589 thrust faults, as it marks the discontinuity between the weak, mobilized mid to lower
590 crustal metamorphic rocks and the stronger rocks of the orogenic allochthonous fore-
591 land which are associated with a fold and thrust belt (Boyer & Elliott, 1982). 3)
592 Beneath the allochthonous foreland, the sole fault separates the orogenic wedge from the
593 underthrust substrate that experiences little internal deformation (Hodges, 2016). In
594 the Himalaya and East Greenland Caledonides, dry Cratonic continental lithosphere
595 was underthrust beneath the orogenic wedge, whereas in Arizona, the Farallon Slab of
596 oceanic affinity was underthrust at a low angle beneath North America and therefore
597 the sole thrust of the orogenic wedge would have localized along the plate interface.

598 CONCLUSIONS

599 We document an inverted metamorphic gradient across the Harcuvar-Harquahala-
600 Granite Wash Mountains which is characteristic of hotter and deeper rocks being
601 thrust on top of colder rocks that were not buried to as great depths. This is further
602 supported by the overlapping timing of top-SW thrusting on the Hercules and Har-
603 quahala Thrusts with top-NE shearing affecting higher-grade metamorphic rocks and
604 migmatites at higher structural levels. These features are consistent with ductile extru-
605 sion or channel flow of mid to lower crustal high-grade metamorphic rock, gneisses
606 and migmatites towards the SW. Southwestward directed flow was likely facilitated
607 by water-fluxed crustal melting and associated rheological weakening of the mid to
608 lower crust. This likely occurred due to the addition of slab-derived volatiles infiltrat-
609 ing across the Moho during low angle subduction of the Farallon slab directly beneath
610 North America.

611 We therefore propose that the ‘ancestral’ top-NE shear fabrics preserved within
612 the Harcuvar-Harquahala-Granite Wash Mountains do not represent crustal exten-
613 sion or ‘orogenic collapse’ but rather the roof shear zone of a mid to lower crustal
614 channel or extruding wedge in an overall contractional setting. This ductile extrusion
615 occurred more than ~ 40 Myrs before regional Cenozoic extension responsible for final
616 MCC exhumation associated with the brittle-ductile Bullard/Eagle Eye Detachments
617 at ca. 22-16 Ma, that potentially reactivated the earlier roof shear zone of this mid to
618 lower crustal channel or wedge (Fig. 9C). Therefore, the Harcuvar-Harquahala-Granite
619 Wash Mountains record pre-extensional orogenic events that have been overprinted or
620 captured by a completely unrelated normal fault (Bullard/ Eagle Eye Detachment)
621 during a more recent phase of regional extension. We therefore suggest that metamor-
622 phic rocks and ductile shear zones exposed within the footwalls of MCCs around the
623 world, especially in cases where ‘extensional’ fabrics may predate recognized regional
624 extension, be carefully re-examined in light of these new data.

625 **Supplementary Information.** Supplementary Material is available using the
626 following link:

627 **Acknowledgments.** This work benefited from numerous discussions with Adam
628 Gorecki, Frances Cooper and particularly Mike Searle. TL thanks Matt Loader, Noah
629 Metz and Joel Leonard for assistance in the field upon first visiting the area during
630 2021-2022. TL thanks Steve Reynolds for an overview discussion of the Harcuvar-
631 Harquahala Mountains and targeted sampling areas for further research. Gordon Haxel
632 and Carl Jacobson are thanked for thought provoking discussion and pointing TL and
633 GE to investigate the PORS at the Gavilan Hills. SS acknowledges analytical assistance
634 from Charles Knaack (WSU RIGL), and funding assistance from NSF-EAR2342159
635 awarded to JH.

636 Declarations

- 637 • Funding: SS acknowledges analytical assistance from Charles Knaack (WSU RIGL),
638 and funding assistance from NSF-EAR2342159 awarded to JH.
- 639 • Competing interests: The authors declare that there is no competing financial
640 interests.
- 641 • Ethics approval: Not Applicable
- 642 • Consent to participate: Not Applicable
- 643 • Consent to publication: Not Applicable
- 644 • Availability of data and materials: Full data and materials are presented in the
645 online Supplementary Material.
- 646 • Code availability: The codes used for petrological modelling are available at:
647 <https://hpxeosandthermocalc.org/the-thermocalc-software/>
- 648 • Authors’ contributions: TL conceived the idea and wrote the first draft. All authors
649 conducted fieldwork and sample collection. SS conducted the U-Pb analyses and
650 TL collected the EPMA data and conducted the thermobarometric calculations. All
651 authors contributed to subsequent drafts.

652 MATERIALS AND METHODS

653 Electron Probe Micro-Analysis (EPMA)

654 The compositions of phases in samples TLAZ22-08 and TLAZ22-167 were presented
655 in Lamont et al. (2024). Additional electron probe micro-analysis (EPMA) were per-
656 formed on sample TL25GH-09 using a CAMECA SX5-FE electron microprobe at the
657 Department of Earth Sciences, University of Oxford. Operating conditions involved
658 an accelerating voltage of 15.0 keV corresponding to a current of 20 nA, a range of
659 primary standards were used, including andradite (Fe, Mg, Ca), TiO₂ (Ti), Mn metal
660 (Mn), labradorite (Na, Al, Si) and sanidine (K) for major elements, and secondary
661 standards include diopside, KK1, SPH Labradorite, RN18 and FDLA1. Garnet line
662 profiles were collected using a 75-100 μm step size across all garnets from rim to rim,
663 equating to \pm 30-50 analyses per garnet. The full results are presented in supplement-
664 ary table S1 and the garnet line chemical profiles are presented in the supplementary
665 material.

666 Thermobarometry

667 P-T calculations on samples TLAZ22-08 and TLAZ22-167 were presented in Lamont
668 et al. (2024). Additional calculations were performed on sample TL25GH-09, a garnet
669 amphibolite from the Orocochia Schist at the Gavilan Hills, SE CA, using Average P-
670 T mode in THERMOCALC version TC-3.40i (Powell and Holland, 1988, 1994) using
671 dataset 62 (Holland & Powell, 2011) with characteristic end members judged to be
672 in textural equilibrium. Activities of phase end-member were calculated using the
673 average phase compositions and garnet core and garnet rim compositions determined
674 by EPMA and running through the program AX62 (last accessed April 2026). The
675 complete results are presented in Supplementary table S2.

676 U–Th–Pb Geochronology

677 Zircon U-Pb isotope measurement at Washington Sate University were performed with
678 a Thermo Element2 HR-ICP-MS connected to a Teledyne Photon Machines Analyte
679 Excite 193 nm ArF laser ablation system. Reference materials were analyzed during the
680 session and typically bracketed every \pm 10 unknown analyses. FC-1 (1099 Ma; Paces
681 & Miller, 1993) and Plešovice (337.1 Ma; Sláma et al., 2008) standards were used as
682 principal reference materials to correct for ²⁰⁷Pb/²⁰⁶Pb and ²⁰⁶Pb/²³⁸U, respectively.
683 Secondary reference materials including 91500 (1065 Ma; Wiedenbeck et al., 1995) were
684 used to evaluate the accuracy of the analyses during each session. The U-Pb isotope
685 data and downhole fractionation corrections were reduced in Iolite v4 (Paton et al.,
686 2010, 2011). The U-Pb ages obtained for each zircon standard in different analytical
687 sessions are within \pm 1 % of their reported “true” age. The full results and concordia
688 plots and are presented in the supplementary material and supplementary table S3.

689 References

690 Andresen A, Hartz EH, Vold J. (1998). A late orogenic extensional origin for

- 691 the infracrustal gneiss domes of the East Greenland Caledonides (72–74°N).
692 *Tectonophysics* 285:353–69
- 693 Bahadori, A., Holt, W. E., & Rasbury, E. T. (2018). Reconstruction modeling of
694 crustal thickness and paleotopography of western North America since 36 Ma.
695 *Geosphere*, 14(3), 1207-1231.
- 696 Barra, F., Ruiz, J., Mathur, R., & Titley, S. (2003). A Re–Os study of sulfide minerals
697 from the Bagdad porphyry Cu–Mo deposit, northern Arizona, USA. *Mineralium*
698 *Deposita*, 38(5), 585-596.
- 699 Barth, A.P., Wooden J.K., Jacobson C.E., & Probst K., (2004). U–Pb geochronology
700 and geochemistry of the McCoy Mountains Formation, southeastern California:
701 A Cretaceous retroarc foreland basin: *Geological Society of America Bulletin*, v.
702 116, p. 142– 153, doi: 10.1130/B25288.1.
- 703 Beaumont, C., Jamieson, R. A., Nguyen, M. H., & Lee, B. (2001). Himalayan tectonics
704 explained by extrusion of a low-viscosity crustal channel coupled to focused surface
705 denudation. *Nature*, 414(6865), 738-742.
- 706 Boyer, S. E., & Elliott, D. (1982). Thrust systems. *AAPG Bulletin* 66, 1196–1230.
707 <https://doi.org/10.1306/03B5A77D-16D1-11D7-8645000102C1865D>
- 708 Bryant, B., & Wooden, J. L. (2008). Geology of the northern part of the Harcuvar
709 complex, west-central Arizona (p. 52). US Geological Survey.
- 710 Burchfiel, B. C., & Royden, L. H., (1985). North-south extension within the convergent
711 Himalayan region: *Geology*, v. 13, p. 679-682.
- 712 Burchfiel, B. C., Zhiliang, C., Hodges, K. V., Yuping, L., Royden, L. H., Changrong,
713 D., & Jiene, X. (1992). The South Tibetan detachment system, Himalayan oro-
714 gen: Extension contemporaneous with and parallel to shortening in a collisional
715 mountain belt.
- 716 Cabby, R. (1983). Le grand chevauchement central himalayaen: Nouvelles donnees sur
717 le metamorphisme inverse a la base de la Dalle du Tibet. *Revue de geologie*
718 *dynamique et de geographie physique*, 24, 89-100.
- 719 Caylor, E. A., Carrapa, B., DeCelles, P. G., & Gehrels, G. E. (2024). The real McCoy:
720 A record of deep-water basin deposition in southwestern North America during
721 the Cretaceous. *Basin Research*, 36(5), e12902.
- 722 Chapman, A. D. (2017). The Pelona–Orocopia–Rand and related schists of southern
723 California: A review of the best-known archive of shallow subduction on the planet.
724 *International Geology Review*, 59(5-6), 664-701.
- 725 Chapman, A. D., Rautela, O., Shields, J., Ducea, M. N., & Saleeby, J. (2020). Fate
726 of the lower lithosphere during shallow-angle subduction: The Laramide example.
727 *GSA Today*, 30(1), 4-10.
- 728 Chapman, J. B., Greig, R., & Haxel, G. B. (2020). Geochemical evidence for an oro-
729 genic plateau in the southern US and northern Mexican Cordillera during the
730 Laramide orogeny. *Geology*, 48(2), 164-168.
- 731 Chapman, J. B., D'Arco, M. N., Gehrels, G., Ducea, M. N., Valley, J. W., & Ishida, A.
732 (2018). Lithospheric architecture and tectonic evolution of the southwestern US
733 Cordillera: Constraints from zircon Hf and O isotopic data. *Bulletin*, 130(11-12),
734 2031-2046.
- 735 Chapman, J. B., Pridmore, C., Chamberlain, K., Haxel, G., & Ducea, M. (2023).

- 736 Himalayan-like crustal melting and differentiation in the southern North Ameri-
737 can Cordilleran anatectic belt during the Laramide orogeny: Coyote Mountains,
738 Arizona. *Journal of Petrology*, 64(10), egad075.
- 739 Cheadle, M. J., B. L. Czuchra, T. Byrne, C. J. Ando, J. E. Oliver, L. D. Brown,
740 S. Kaufman, P. E. Malin, and R. A. Phinney (1986), The deep crustal structure
741 of the Mojave Desert, California, from Cocorp seismic reflection data, *Tectonics*,
742 5(2), 293–320, doi:10.1029/TC005i002p00293.
- 743 Cottle, J. M., Jessup, M. J., Newell, D. L., Searle, M. P., Law, R. D., & Horstwood, M.
744 S. (2007). Structural insights into the early stages of exhumation along an orogen-
745 scale detachment: The South Tibetan Detachment System, Dzaka Chu section,
746 Eastern Himalaya. *Journal of Structural Geology*, 29(11), 1781-1797.
- 747 Cottle, J. M., Jessup, M. J., Newell, D. L., Horstwood, M. S., Noble, S. R., Parrish,
748 R. R., ... & Searle, M. P. (2009). Geochronology of granulitized eclogite from the
749 Ama Drime Massif: Implications for the tectonic evolution of the South Tibetan
750 Himalaya. *Tectonics*, 28(1).
- 751 Cottle, J. M., Searle, M. P., Jessup, M. J., Crowley, J. L., & Law, R. D. (2015).
752 Rongbuk re-visited: Geochronology of leucogranites in the footwall of the South
753 Tibetan detachment system, Everest region, southern Tibet. *Lithos*, 227, 94-106.
- 754 Dalmayrac, B., & Molnar, P. (1981). Parallel thrust and normal faulting in Peru and
755 constraints on the state of stress. *Earth and Planetary Science Letters*, 55(3),
756 473-481.
- 757 Dewey, J. F. (1988). Extensional collapse of orogens. *Tectonics*, 7(6), 1123-1139.
- 758 Dyck, B., Waters, D. J., St-Onge, M. R., & Searle, M. P. (2020). Muscovite dehydration
759 melting: Reaction mechanisms, microstructures, and implications for anatexis.
760 *Journal of Metamorphic Geology*, 38(1), 29-52.
- 761 Elvevold, S., Thrane, K., Gilotti, J., A. (2003). Metamorphic history of high-pressure
762 granulites in Payer Land, Greenland Caledonides. *Journal of Metamorphic
763 Geology*. 21, 49–63.
- 764 England, P. C., and Holland, T.J., (1979). Archimedes and the Tauern eclogites: the
765 role of buoyancy in the preservation of exotic eclogite blocks, *Earth and Planetary
766 Science Letters*, 44, 2, 287-294, DOI : 10.1016/0012-821X(79)90177-8
- 767 English, J. M., Johnston, S. T., & Wang, K. (2003). Thermal modelling of the
768 Laramide orogeny: testing the flat-slab subduction hypothesis. *Earth and Plane-
769 tary Science Letters*, 214(3-4), 619-632.
- 770 Favorito, D. A., & Seedorff, E. (2024). Temporal and spatial relations between por-
771 phyry copper deposits and crustal shortening: Insights from the Laramide arc of
772 Arizona and New Mexico. *Economic Geology*, 119(6), 1261-1288.
- 773 Fornash, K. F., Patchett, P. J., Gehrels, G. E., & Spencer, J. E. (2013). Evo-
774 lution of granitoids in the Catalina metamorphic core complex, southeastern
775 Arizona: U–Pb, Nd, and Hf isotopic constraints. *Contributions to Mineralogy and
776 Petrology*, 165(6), 1295-1310.
- 777 Gerya, T. V., Stöckhert, B., & Perchuk, A. L. (2002). Exhumation of high-pressure
778 metamorphic rocks in a subduction channel: A numerical simulation, *Tectonics*,
779 21(6), 1056, doi:10.1029/2002TC001406
- 780 Gilotti, J., A., McClelland, W. C., (2005). Leucogranites and the time of extension in

- 781 the East Greenland Caledonides. *Journal of Metamorphic Geology*, 113, 399–417.
782 Gilotti J. A., Jones, K. A., & Elvevold, S. (2008). Caledonian metamorphic patterns
783 in Greenland. *Geological Society America Memoirs* 202, 201–25.
784 Godin, L., Grujic, D., Law, R. D., & Searle, M. P. (2006). Channel flow, ductile
785 extrusion and exhumation in continental collision zones: an introduction.
786 Golos, E. M., & Fischer, K. M. (2022). New insights into lithospheric structure and
787 melting beneath the Colorado Plateau. *Geochemistry, Geophysics, Geosystems*,
788 23(3), e2021GC010252. doi.org
789 Grujic, D., Casey, M., Davidson, C., Hollister, L. S., Kündig, R., Pavlis, T., & Schmid,
790 S. (1996). Ductile extrusion of the Higher Himalayan Crystalline in Bhutan:
791 evidence from quartz microfabrics. *Tectonophysics*, 260(1-3), 21-43.
792 Harris, N., & Massey, J. (1994). Decompression and anatexis of Himalayan metapelites.
793 *Tectonics*, 13(6), 1537-1546.
794 Hartz, E., & Andresen, A. (1995). Caledonian sole thrust of central East Greenland:
795 a crustal-scale Devonian extensional detachment? *Geology* 23:637–40
796 Hartz, E. H., Andresen, A., Hodges K. V., & Martin M. W., (2001). Syncontractional
797 extension and exhumation of deep crustal rocks in the east Greenland Caledonides.
798 *Tectonics* 20:58–77
799 Hartz E. H., Andresen A., Martin M. W., & Hodges K. V. (2000). U-Pb and ⁴⁰Ar/³⁹Ar
800 constraints on the Fjord Region detachment zone: a long-lived extensional fault in
801 the East Greenland Caledonides. *Journal of the Geological Society London*, 157,
802 795–809.
803 Hodges, K. V. (2016). Crustal decoupling in collisional orogenesis: examples from
804 the East Greenland Caledonides and Himalaya. *Annual Review of Earth and*
805 *Planetary Sciences*, 44, 685-708.
806 Hodges, K. V., & Walker, J. D. (1992). Extension in the Cretaceous Sevier orogen,
807 North American Cordillera. *Geological Society of America Bulletin*, 104(5), 560-
808 569.
809 Holland, T. J. B. & Powell, R. (2011). An improved and extended internally consist-
810 ent thermodynamic dataset for phases of petrological interest, involving a new
811 equation of state for solids. *Journal of Metamorphic Geology*, 29(3), 333-383.
812 Hopkinson, T., Harris, N., Roberts, N. M., Warren, C. J., Hammond, S., Spencer, C.
813 J., & Parrish, R. R. (2020). Evolution of the melt source during protracted crustal
814 anatexis: An example from the Bhutan Himalaya. *Geology*, 48(1), 87-91.
815 Howard, K. A., Dennis, M. L., Karlstrom, K., & Phelps, G. A. (1997). Preliminary
816 geologic map of the Little Piute Mountains, California: A digital database (No.
817 97-693). US Geological Survey.
818 Hubbard, M. S. (1989). Thermobarometric constraints on the thermal history of the
819 Main Central Thrust Zone and Tibetan Slab, eastern Nepal Himalaya. *Journal of*
820 *Metamorphic Geology*, 7(1), 19-30.
821 Isachsen, C. E., Gehrels, G. E., Riggs, N. R., Spencer, J. E., Ferguson, C. A., Skotnicki,
822 S. J., & Richard, S. M. (1999). U-Pb geochronologic data from zircons from eleven
823 granitic rocks in central and western Arizona.
824 Jacobson, C. E., Grove, M., Vucic, A., Pedrick, J. N., & Ebert, K. A. (2007). Exhuma-
825 tion of the Orocopia Schist and associated rocks of southeastern California:

- 826 Relative roles of erosion, synsubduction tectonic denudation, and middle Cenozoic
827 extension.
- 828 Jamieson, R. A., Unsworth, M. J., Harris, N. B., Rosenberg, C. L., & Schulmann, K.
829 (2011). Crustal melting and the flow of mountains. *Elements*, 7(4), 253-260.
- 830 Johnston, S., M., & Kylander-Clark, A., R., C., (2013). Discovery of an Eo-Meso-
831 Neoproterozoic terrane in the East Greenland Caledonides. *Precambrian Research*,
832 235, 295–302.
- 833 Kalsbeek, F., Jepsen, H. F., & Nutman, A. P., (2001). From source migmatites to
834 plutons: tracking the origin of ca. 435 Ma S-type granites in the East Greenland
835 Caledonian orogen. *Lithos* 57, 1–21.
- 836 Kapp, P., Jepsen, G., Carrapa, B., Schaen, A. J., He, J. J. Y., & Wang,
837 J. W. (2023). Laramide bulldozing of lithosphere beneath the Arizona
838 transition zone, southwestern United States. *Geology*, 51(10), 952–956.
839 <https://doi.org/10.1130/G51194.1>
- 840 Keith, S., C. Rasmussen, J., & Spieth, V. (2026). A New Class of
841 Nonvolcanic, Large, Peraluminous Copper-Oxide Greisen Deposits
842 in Arizona, USA. In *Latest Advances in Volcanology*. IntechOpen.
843 <https://doi.org/10.5772/intechopen.1014159>
- 844 Klemperer, S. L. (2006). Crustal flow in Tibet: geophysical evidence for the physical
845 state of Tibetan lithosphere, and inferred patterns of active flow.
- 846 Knapp, J. H., and Heizler, M. T., (1987), Thermal History of Crystalline Nappes of
847 the Maria Fold and Thrust Belt, West Central Arizona, *Journal of Geophysical*
848 *Research*, v. 95, no. B12, p. 20049-20073.
- 849 Laccarino, S., Montomoli, C., Carosi, R., Massonne, H. J., Langone, A., &
850 Visonà, D. (2015). Pressure–temperature–time–deformation path of kyanite-
851 bearing migmatitic paragneiss in the Kali Gandaki valley (Central Nepal):
852 Investigation of Late Eocene–Early Oligocene melting processes. *Lithos*, 231,
853 103-121.
- 854 Lamont, T. N., Searle, M. P., Waters, D. J., Roberts, N. M., Palin, R. M., Smye, A., ...
855 & St-Onge, M. R. (2020a). Compressional origin of the Naxos metamorphic core
856 complex, Greece: Structure, petrography, and thermobarometry. *GSA Bulletin*,
857 132(1-2), 149-197.
- 858 Lamont, T. N., Searle, M. P., Gopon, P., Roberts, N. M., Wade, J., Palin, R. M., &
859 Waters, D. J. (2020b). The Cycladic Blueschist Unit on Tinos, Greece: Cold NE
860 subduction and SW directed extrusion of the Cycladic continental margin under
861 the Tsiknias Ophiolite. *Tectonics*, 39(9), e2019TC005890.
- 862 Lamont, T. N., Smye, A. J., Roberts, N. M., Searle, M. P., Waters, D. J., & White,
863 R. W. (2023). Constraints on the thermal evolution of metamorphic core com-
864 plexes from the timing of high-pressure metamorphism on Naxos, Greece. *Bulletin*,
865 135(11-12), 2767-2796.
- 866 Lamont, T. N., Roberts, N. M., Searle, M. P., Gardiner, N. J., Gopon, P., Hsieh, Y. T.,
867 ... & White, R. W. (2023). Contemporaneous crust-derived I-and S-type granite
868 magmatism and normal faulting on Tinos, Delos, and Naxos, Greece: Constraints
869 on Aegean orogenic collapse. *Bulletin*, 135(11-12), 2797-2829.
- 870 Lamont, T. N., Loader, M. A., Roberts, N. M., Cooper, F. J., Wilkinson, J. J., Bevan,

- 871 D., ... & Tapster, S. (2024). Porphyry copper formation driven by water-fluxed
872 crustal melting during flat-slab subduction. *Nature Geoscience*, 17(12), 1306-1315.
- 873 Laubach, S. E., Reynolds, S. J., Spencer, J. E., & Marshak, S. (1989). Progressive
874 deformation and superposed fabrics related to Cretaceous crustal underthrusting
875 in western Arizona, USA. *Journal of Structural Geology*, 11(6), 735-749.
- 876 Law, R. D., Searle, M. P., & Simpson, R. L. (2004). Strain, deformation temperatures
877 and vorticity of flow at the top of the Greater Himalayan Slab, Everest Massif,
878 Tibet. *Journal of the Geological Society*, 161(2), 305-320.
- 879 Law, R. D., Jessup, M. J., Searle, M. P., Francis, M. K., Waters, D. J., & Cottle,
880 J. M. (2011). Telescoping of isotherms beneath the South Tibetan detachment
881 system, Mount Everest Massif. *Journal of Structural Geology*, 33(11), 1569-1594.
- 882 McClay KR, Norton MG, Coney P, & Davis GH. (1986). Collapse of the Caledonian
883 orogen and the Old Red Sandstone. *Nature* 323, 147-49.
- 884 Means, W.D. (1989). Stretching faults. *Geology*, 17, 893-896.
- 885 Paces, J. B., & Miller, J. D., Jr. (1993). Precise U-Pb ages of Duluth Complex and
886 related mafic intrusions, northeastern Minnesota: Geochronological insights into
887 physical, chemical, and tectonic controls on midcontinent rift magmatism. *Journal*
888 *of Geophysical Research: Solid Earth*, 98(B8), 13997-14013.
- 889 Patiño Douce, A.E., and Harris, N., (1998), Experimental constraints
890 on Himalayan Anatexis: *Journal of Petrology* , v. 39, p. 689-710,
891 <https://doi.org/10.1093/petroj/39.4.689>.
- 892 Paton, C., Woodhead, J. D., Hellstrom, J. C., Hergt, J. M., Greig, A., & Maas,
893 R. (2010). Improved laser ablation U-Pb zircon geochronology through robust
894 downhole fractionation correction. *Geochemistry, Geophysics, Geosystems*, 11(3).
- 895 Paton, C., Hellstrom, J., Paul, B., Woodhead, J., & Hergt, J. (2011). Iolite: Free-
896 ware for the visualisation and processing of mass spectrometric data. *Journal of*
897 *Analytical Atomic Spectrometry*, 26(12), 2508-2518.
- 898 Platt, J. P., Behr, W. M., & Cooper, F. J. (2015). Metamorphic core complexes:
899 Windows into the mechanics and rheology of the crust. *Journal of the Geological*
900 *Society*, 172(1), 9-27.
- 901 Powell, R., & Holland, TJB, (1988). An internally consistent thermodynamic dataset
902 with uncertainties and correlations: 3: application methods, worked examples and
903 a computer program. *Journal of Metamorphic Geology* 6, 173-204.
- 904 Powell, R., & Holland, TJB, (1994). Optimal geothermometry and geobarometry.
905 *American Mineralogist* 79, 120-133.
- 906 Priestley, K., Jackson, J., & McKenzie, D. (2008). Lithospheric structure and deep
907 earthquakes beneath India, the Himalaya and southern Tibet. *Geophysical Journal*
908 *International*, 172(1), 345-362.
- 909 Rehrig W, Shafiqullah M, Damon P, (1980). Geochronology, geology and listric normal
910 faulting of the Vulture Mountains, Maricopa County, Arizona. In: Jenney J, Stone
911 C, editors. *Studies in Western Arizona*. Tucson: Arizona Geological Society Digest;
912 1980. Vol. 12. p. 89-110.
- 913 Reynolds, S. J., & Spencer, J. E. (1985). Evidence for large-scale transport on the
914 Bullard detachment fault, west-central Arizona. *Geology*, 13(5), 353-356.
- 915 Reynolds, S. J., & Lister, G. S. (1990). Folding of mylonitic zones in Cordilleran

- 916 metamorphic core complexes: Evidence from near the mylonitic front. *Geology*,
917 18(3), 216-219.
- 918 Reynolds, S.J., Spencer, J.E., & DeWitt, E., (1987). Stratigraphy and U-Th-Pb
919 geochronology of Triassic and Jurassic rocks in west-central Arizona, in Dickin-
920 son, W.R., and Klute, M.A., eds., *Mesozoic rocks of central and southern Arizona*
921 and adjacent areas: Arizona Geological Society Digest, vol. 18, p. 65-80.
- 922 Richard, S. M., Ballard, S. N., Boettcher, S. S., Hamilton, W. B., Hoisch, T. D., &
923 Tosdal, R. M., (1994), *Mesozoic Tectonics of the Maria Belt, west-central Arizona*
924 and southeastern California, in S. F. McGill and Ross, T. M., eds., *Geological*
925 *Investigations of an Active Margin*. Edited by Geological Society of America Field
926 trip Guidebook. San Bernardino, CA: County Museum Association, 1994, pp.
927 272-292.
- 928 Royden, L. (1996). Coupling and decoupling of crust and mantle in convergent orogens:
929 Implications for strain partitioning in the crust. *Journal of Geophysical Research:*
930 *Solid Earth*, 101(B8), 17679-17705.
- 931 Royden, L., & Keen, C. E. (1980). Rifting process and thermal evolution of the conti-
932 nental margin of eastern Canada determined from subsidence curves. *Earth and*
933 *Planetary Science Letters*, 51(2), 343-361.
- 934 Rosenberg, C.L. and Handy, M.R. (2005), Experimental deformation of partially
935 melted granite revisited: implications for the continental crust. *Journal of Meta-*
936 *morphic Geology*, 23: 19-28. <https://doi.org/10.1111/j.1525-1314.2005.00555.x>
- 937 Ruppel, C., Royden, L., & Hodges, K. V. (1988). Thermal modeling of extensional tec-
938 tonics: Application to pressure-temperature-time histories of metamorphic rocks.
939 *Tectonics*, 7(5), 947-957.
- 940 Salem, A.C., 2009, *Mesozoic tectonics of the Maria fold and thrust belt and McCoy*
941 *basin an examination of polyphase deformation and synorogenic response*, PhD
942 Thesis: University of New Mexico, Dept. of Earth and Planetary Sciences,
943 Albuquerque, NM, USA.
- 944 Scoggin, S. H., Chapman, J. B., Shields, J. E., Trzinski, A. E., & Ducea, M. N. (2021).
945 Early Paleogene Magmatism in the Pinaleno Mountains, Arizona: evidence for
946 crustal melting of diverse basement assemblages during the Laramide orogeny.
947 *Journal of Petrology*, 62(12), egab095.
- 948 Searle, M. P. (2010). Low-angle normal faults in the compressional Himalayan orogen;
949 Evidence from the Annapurna–Dhaulagiri Himalaya, Nepal. *Geosphere*, 6(4), 296-
950 315.
- 951 Searle, M. P., & Lamont, T. N. (2020). Compressional metamorphic core complexes,
952 low-angle normal faults and extensional fabrics in compressional tectonic settings.
953 *Geological Magazine*, 157(1), 101-118.
- 954 Searle, M. P., & Lamont, T. N. (2022). Compressional origin of the Aegean orogeny,
955 Greece. *Geoscience Frontiers*, 13(2), 101049.
- 956 Searle, M. P., & Rex, A. J. (1989). Thermal model for the Zaskar Himalaya. *Journal*
957 *of Metamorphic Geology*, 7(1), 127-134.
- 958 Searle, M. P., Simpson, R. L., Law, R. D., Parrish, R. R., & Waters, D. J. (2003). The
959 structural geometry, metamorphic and magmatic evolution of the Everest massif,
960 High Himalaya of Nepal–South Tibet. *Journal of the Geological Society*, 160(3),
961 345-366.

- 962 Singleton, J. S., D. F. Stockli, P. B. Gans, and M. G. Prior (2014). Timing, rate,
963 and magnitude of slip on the Buckskin-Rawhide detachment fault, west-central
964 Arizona, *Tectonics*, 33, 1596–1615, doi:10.1002/2013TC003517.
- 965 Sláma, J., Košler, J., Condon, D. J., Crowley, J. L., Gerdes, A., Hanchar, J. M., ... &
966 Whitehouse, M. J. (2008). Plešovice zircon—a new natural reference material for
967 U–Pb and Hf isotopic microanalysis. *Chemical geology*, 249(1-2), 1-35.
- 968 Spear, F. S., & Pyle, J. M. (2002). Apatite, monazite, and xenotime in metamorphic
969 rocks.
- 970 Spear, F. S., & Pyle, J. M. (2010). Theoretical modeling of monazite growth in a
971 low-Ca metapelite. *Chemical Geology*, 273(1-2), 111-119.
- 972 Spencer, J. E., & Reynolds, S. J. (1990). Relationship between Mesozoic and Cenozoic
973 tectonic features in west central Arizona and adjacent southeastern California.
974 *Journal of Geophysical Research: Solid Earth*, 95(B1), 539-555.
- 975 Spencer, J. E., Richard, S. M., & Reynolds, S. J. (2024). Geologic map of the Little
976 Harquahala Mountains, west-central Arizona (v. 2.0, DGM-203) [Map]. Arizona
977 Geological Survey.
- 978 Strachan R.A. (1994). Evidence in North-East Greenland for Late Silurian–Early
979 Devonian regional extension during the Caledonian orogeny. *Geology* 22:913–16
- 980 Strachan, R. A., & Martin M. W., (2001). Evidence for contemporaneous yet con-
981 trasting styles of granite magmatism during extensional collapse of the northeast
982 Greenland Caledonides. *Tectonics*, 20, 458–73.
- 983 Strickland, E. D., Singleton, J. S., & Haxel, G. B. (2018). Orocopia Schist in the north-
984 ern Plomosa Mountains, west-central Arizona: A Laramide subduction complex
985 exhumed in a Miocene metamorphic core complex. *Lithosphere*, 10(6), 723-742.
- 986 Teyssier, C., & Whitney, D. L. (2002). Gneiss domes and orogeny. *Geology*, 30(12),
987 1139-1142.
- 988 Walsh, E. O., Wong, M. S., Singleton, J. S., Wrobel, A. J., Weiss, T., & Christensen,
989 K. (2016). Evidence for polyphase exhumation of the Harcuvar metamorphic
990 core complex, western Arizona. *Geological Society of America Abstracts with*
991 *Programs*, 48(7), 287659. <https://doi.org/10.1130/abs/2016AM-287659>
- 992 Waters, D. J., Law, R. D., Searle, M. P., & Jessup, M. J. (2019). Structural and
993 thermal evolution of the South Tibetan Detachment shear zone in the Mt Everest
994 region, from the 1933 sample collection of LR Wager. *Geological Society, London,*
995 *Special Publications*, 478(1), 335-372.
- 996 Watt, G. R., Kinny, P. D., & Friderichsen, J. D. (2000). U–Pb geochronology of
997 Neoproterozoic and Caledonian tectonothermal events in the East Greenland
998 Caledonides. *Journal of the Geological Society*, 157(5), 1031-1048.
- 999 Weinberg, R. F., & Hasalová, P. (2015). Water-fluxed melting of the continental crust:
1000 a review. *Lithos*, 212, 158-188.
- 1001 Wells, M. L., & Hoisch, T. D. (2008). The role of mantle delamination in widespread
1002 Late Cretaceous extension and magmatism in the Cordilleran orogen, western
1003 United States. *Geological Society of America Bulletin*, 120(5-6), 515-530.
- 1004 Whitney, D. L., Teyssier, C., Rey, P., & Buck, W. R. (2013). Continental and oceanic
1005 core complexes. *Geological Society of America Bulletin*, 125(3-4), 273-298.
- 1006 Yang, L., Zeng, L., Wang, J., Gao, L., & Guo, C. (2019). Is Himalayan leucogranite

1007 a product by in situ partial melting of the Greater Himalayan Crystalline? A
1008 comparative study of leucosome and leucogranite from Nyalam, southern Tibet.
1009 *Lithos*, 344–345, 105124. DOI: 10.1016/j.lithos.2019.105124
1010 White AP, Hodges KV. (2002). Multistage extensional evolution of the central East
1011 Greenland Caledonides. *Tectonics* 21:1048
1012 White AP, Hodges KV. (2003). Pressure-temperature-time evolution of the central
1013 East Greenland Caledonides: quantitative constraints on crustal thickening and
1014 synorogenic extension. *J. Metamorph. Geol.* 21:875–97
1015 White AP, Hodges KV, Martin MW, Andresen A. (2002). Geologic constraints on
1016 middle-crustal behavior during broadly synorogenic extension in the central East
1017 Greenland Caledonides. *Int. J. Earth Sci.* 91:187–208
1018 Wiedenbeck, M. A. P. C., Alle, P., Corfu, F. Y., Griffin, W. L., Meier, M., Oberli, F.
1019 V., ... & Spiegel, W. (1995). Three natural zircon standards for U-Th-Pb, Lu-Hf,
1020 trace element and REE analyses. *Geostandards newsletter*, 19(1), 1-23.
1021 Wong, M. S., Singleton, J. S., Seymour, N. M., Gans, P. B., & Wrobel, A. J. (2023).
1022 Late Cretaceous-Early Paleogene Extensional Ancestry of the Harcuvar and
1023 Buckskin-Rawhide Metamorphic Core Complexes, Western Arizona. *Tectonics*,
1024 42(2), e2022TC007656.